Comparative analyses for determining shallow water bathymetry potential of multispectral UAVs: case study in Tavşan Island, Sea of Marmara

Umut Gunes Sefercik[1]*, Mertcan Nazar[1], Ilyas Aydin[1], Gürcan Büyüksalih[2], Cem Gazioglu[2] and Irsad Bayirhan[2]

[1]Department of Geomatics Engineering, Faculty of Engineering, Gebze Technical University, Kocaeli, Türkiye, [2]Department of Marine Environment, Institute of Marine Sciences and Management, Istanbul University, Istanbul, Türkiye

Recently, the use of unmanned aerial vehicles (UAVs) in bathymetric applications has become very popular due to the rapid and periodic acquisition of high spatial resolution data that provide detailed modeling of shallow water body depths and obtaining geospatial information. In UAV-based bathymetry, the sensor characteristics, imaging geometries, and the quality of radiometric and geometric calibrations of the imagery are the basic factors to achieve most reliable results. Digital bathymetric models (DBMs) that enable three-dimensional bottom topography definition of water bodies can be generated using many different techniques. In this paper, the effect of different UAV imaging bands and DBM generation techniques on the quality of bathymetric 3D modeling was deeply analyzed by visual and statistical model-based comparison approaches utilizing reference data acquired by a single-beam echosounder. In total, four different DBMs were generated and evaluated, two from dense point clouds derived from red−green−blue (RGB) single-band and multispectral (MS) five-band aerial photos, and the other two from Stumpf and Lyzenga empirical satellite-based bathymetry (SDB) adapted to UAV data. The applications were performed in the Tavşan Island located in Istanbul, Turkey. The results of statistical model-based analyses demonstrated that the accuracies of the DBMs are arranged as RGB, MS, Lyzenga, and Stumpf from higher to lower and the standard deviation of height differences are between ±0.26 m and ±0.54 m. Visual results indicate that five-band MS DBM performs best in identifying the deepest areas.

KEYWORDS

UAV, RGB, MS, Stumpf, Lyzenga, digital bathymetric model (DBM), accuracy

1 Introduction

All over the world, coastal zones are in constant development and alteration because of natural processes (Neeman et al., 2015) and human-centered actions (Halpern et al., 2008). Responsible factors for changes in coastal zones may be categorized as geological including the type of sediment, distribution and resistance of sediment formations, and isostasy; geomorphological; hydrodynamic; biological including the effect of plants; climatic including rainfall and wind dynamics; and anthropogenic including settlements, industrial expansion, agricultural activities, deforestation, and conservation of coastal areas (Labuz, 2015). Coastal systems additionally have a dynamic structure and generally react in a non-linear morphological way to change (Dronkers, 2005). Also, coastal zones are an essential part of human life due to the fact that approximately 40% of the world's population live within 100 km of the coast zones and 10% live inside coastal areas that are below 10 m above sea level (United Nations, 2017). Throughout the twentieth century, the global sea level rose at a rate of approximately 1.7 ± 0.5 mm/year, whereas the global ocean temperature has increased by 0.10°C from the water surface to the 700-m depth over the period between 1961 and 2003 (Bindoff et al., 2007). Therefore, monitoring of coastal zones can be an important task for coastal zone protection, well-being of people living inside these zones, and economic activities related to water resources. Periodic observation of coastal areas is also important for the detection of sediment transport, erosion, and accretion (Bio et al., 2015; Kavzoglu et al., 2021; Colkesen et al., 2023). The production of bathymetric maps is also an important task for monitoring marine environment. Depth information and mapping of the water body in coastal areas is critical for many fields of study such as coastal zone management and safety, navigation, oceanography, dredging planning, and construction of marine infrastructure facilities (Muzirafuti et al., 2020; Specht et al., 2020; Alevizos and Alexakis, 2022b). Various technologies and methods have been utilized over the years for bathymetry studies in coastal areas (Lubczonek et al., 2021).

In traditional methods, depth is measured with the help of a pole. With the accumulation of knowledge and developing devices over time, echosounders that form the basis of hydrographic studies have been produced. Echosounders with two different models, single-beam and multi-beam, have been a popular source for determining the depth of a body of water. Multi-beam echosounders can cover the entire seabed with their large swath widths and require a relatively short time for data acquisition (Wlodarczyk-Sielicka and Stateczny, 2016). Some studies have emphasized the disadvantages of these technologies such as cost, high labor requirements, difficulty in data processing, and narrow coverage in shallow waters. Therefore, alternative methods have been proposed for bathymetry measurements (Alvarez et al., 2018; He et al., 2022).

Airborne or space-borne remote sensing methods are relatively low-cost means of data acquisition for monitoring water areas. Airborne laser bathymetry (ALB) has developed rapidly in recent years and has become a widely used resource for bathymetry measurements (Wang and Philpot, 2007; Niemeyer and Sörgel, 2013; Mandlburger, 2019). ALB works with a green laser that can penetrate water bodies. Depth information is calculated based on the values between the water surface and the laser beam reflected

from the water floor. The fact that ALB devices can be used as hybrid sensor systems together with digital cameras also increases the potential of bathymetric measurements (Mandlburger et al., 2021). However, factors such as water turbidity, wind, and seabed condition affect the working principle of this technology and cause limitations. Satellite-derived bathymetry (SDB) studies are also carried out by processing multispectral (MS) space-borne imagery. The SDB method is a much more economical resource for researchers than conventional and airborne laser technologies. The first study using satellites was carried out by NASA in 1975, and the depth of the Bahamas was calculated to approximately 20 m using the MS images of the Landsat 1 satellite. Recent advancements in satellite technology have ushered in a new era for the field of SDB, with cutting-edge satellites like WorldView-2 and -3 and QuickBird leading the way. These state-of-the-art satellites are equipped with high-resolution and MS sensors, presenting unparalleled opportunities for advancements in underwater terrain mapping and bathymetric applications (Belcore and Di Pietra, 2022). The MS sensors on these satellites enable the capture of data across different wavelengths, enhancing the ability to discriminate between various water depths and seafloor characteristics. Energy of different electromagnetic wavelengths can penetrate the water surface, and information about depths at different levels can be obtained (Philpot, 1989). Light with a long wavelength is absorbed faster than light with a short wavelength. The blue band, with its low wavelength and high energy, has a high ability to penetrate more deeply water bodies and is suitable for extracting more information for water regions. The near-infrared (NIR) band is often used for shoreline extraction because it produces low reflectance values for water areas (Jagalingam et al., 2015; Randazzo et al., 2020; Celik and Gazioglu, 2022). Pollution, water turbidity, and atmospheric effects are highly influential in the bathymetric use of satellites with passive sensors (Gao et al., 2007). SDB has a coarser resolution than ALB and does not produce information with sufficient accuracy for specific studies (Jegat et al., 2016; Cao et al., 2019).

In recent years, unmanned aerial vehicle (UAV) has become an alternative technology for remote sensing community with the advantage of very high-resolution data achieved from lower flight altitudes, and low cost (Toro and Tsourdos, 2018; Casella et al., 2022). Today, UAVs are actively used in solving many problems by rapid observations about the relevant areas (Mulsow et al., 2018; Nex et al., 2022; Sefercik et al., 2022). This advantage of UAV makes it highly effective in studies on the analysis of water bodies such as water failure monitoring (Kim et al., 2023), oil spill detection (De Kerf et al., 2020), monitoring of pollution source (Cai et al., 2023), and determination of concentrations of physiochemical parameters in water (Ozdogan et al., 2021; Isgro et al., 2022). Current developments in UAV sensing technologies and data processing techniques have made it possible to imaging and modeling of the seafloor. The processing of high-resolution imagery with the help of the structure from motion (SfM) approach, the development of high-accuracy point clouds, and surface models produced from these data have paved the way for the use of UAVs in underwater areas such as bathymetric mapping (Starek and Giessel, 2017). The presence of rocks at specific elevations along the coastline poses a significant hindrance to smooth ship

movement, thereby underscoring the practical utility of employing UAVs for bathymetric studies. Bathymetric mapping using UAVs emerges as a notably cost-effective alternative source, particularly in the case of clear waters below 10 m in depth, when contrasted with ship-borne echo sounding or underwater photogrammetric methods (Agrafiotis et al., 2018; Alevizos et al., 2022b). UAVs offer numerous advantages, such as swift data acquisition across expansive areas, cost-effective alternatives to traditional methods, and minimal labor requirements for conducting bathymetric measurements (Rossi et al., 2020; Slocum et al., 2020; Alevizos et al., 2022a). In addition to providing depth data based on image-based bathymetric mapping, it also provides simultaneous acquisition of many data with the help of spectral information contained in the image and indices derived from them. In light of the aforementioned advantages, the UAV-derived bathymetry (UDB) method (Rossi et al., 2020), which builds upon the foundations of traditional SDB, is increasingly being adopted in the shallow bathymetry mapping. Recently, learning-based methods, including deep convolutional neural network (Alevizos et al., 2022a), gene-expression programming (Lee et al., 2022), and support vector regression (Specht et al., 2023), have been employed in the field of UDB studies. Nevertheless, empirical SDB methods are still employed in UDB studies, offering reasonable results in shallow bathymetry mapping (Rossi et al., 2020; Specht et al., 2022; Alevizos and Alexakis, 2022a; Apicella et al., 2023).

The accuracy of bathymetry data is significant for a large variety of marine-related applications such as monitoring of sand mobility, coastal erosion, and hydrodynamic structure in the coastal zone, and maritime navigation (Muzirafuti et al., 2020; Doukari et al., 2021; Alevizos and Alexakis, 2022a; Lange et al., 2023). Like any data acquisition technique, the UAV bathymetry has limitations and it should be taken into consideration that bathymetric mapping performed with UAV cannot produce results as consistent as *in-situ* measurements (Santos et al., 2023). In this context, it is necessary to consider factors affecting the accuracy of bathymetry data. In shallow bathymetric mapping, a key limitation is the influence of refraction caused by bending of electromagnetic energy or light as it passes through the water surface, causing the apparent depth to be shallower than the actual depth (Tewinkel, 1963; Harris and Umbach, 1972; Dietrich, 2017; Cao et al., 2019). To overcome this problem, various refraction correction approaches have been developed in recent years for SfM point clouds and UDB models (Woodget et al., 2015; Dietrich, 2017; Agrafiotis et al., 2019, 2020; Lambert and Parrish, 2023; Lingua et al., 2023). A straightforward refractive correction method (Westaway et al., 2000) was employed in Woodget et al. (2015) by multiplying apparent depths, calculated using an underlying digital elevation model (DEM) and estimated water surface elevations, by the refractive index of clear water, thus obtaining corrected water depths with an error reduction from 16 mm–89 mm to 8 mm–53 mm. Dietrich (2017) proposed an iterative approach for off-nadir multiview stereo photogrammetry, based on calculating a set of equations for each point/camera combination in the point cloud. Compared with the approach applied in Woodget et al. (2015), this iterative approach is also applicable to off-nadir photos, which in turn provides higher accuracy and precision, as well as better camera calibration results (James and Robson, 2014; Carbonneau and Dietrich, 2016). The

iterative approach proposed in Dietrich, (2017) was also applied in a shallow stream bathymetry by Lingua et al. (2023) through the usage of raster data instead of point cloud. The results were satisfactory, with accuracies and precisions of ~0.019% and ~0.07%, respectively, of the flying height. Among these approaches is a learning-based refraction correction approach, DepthLearn, which employs an SVR model developed on the basis of known depth values to correct the systematically underestimated depth values present in the SfM point cloud (Agrafiotis et al., 2019, 2020). Moreover, the SVR model trained on synthetic UAV data with varying flight heights, depths, and seabed anaglyphs displayed notable performance in the correction of estimated depth values while reducing the root mean square error (RMSE) in the z-direction in the range between 7 cm and 24 cm (Agrafiotis et al., 2021). In a recent study, Lambert and Parrish (2023) modified the well-known Stumpf algorithm to test the effect of refraction correction on UAV data. The results demonstrated that the modified algorithm significantly improved accuracy, reducing the RMSE by 3 cm–11 cm.

In this paper, the effect of various UAV imaging bands and different DBM generation methods on the bathymetric 3D modeling quality was comprehensively analyzed through visual and statistical model-based comparison approaches using reference bathymetry data obtained via a single-beam echosounder. Accordingly, four different DBMs were generated and evaluated, two of which were generated using dense point clouds acquired from single-band red–green–blue (RGB) and MS five-band aerial photos, and the other two were generated utilizing Stumpf and Lyzenga empirical SDB models adapted to UAV data. Moreover, the most suitable two-by-two band pair for the Stumpf log-band ratio was determined by means of optimal band ratio analysis (OBRA) and refraction correction was applied to generate SfM point clouds.

2 Study area and materials

Tavşan Island is located at the 2-km South of Büyükada in the Sea of Marmara, Istanbul, Turkey. Marmara is an 11,000-km² inland sea, and seven cities bordering it have vital importance for the country's economy with industrial, trade, tourism, and agricultural activities. The area of Tavşan Island is 3.6 ha, and the elevation reaches up to 30 m from the sea level. The coastal length of the island is approx. 1 km, and the average depth is around 5 m. The Island is home to a diverse range of marine life, including fish, dolphins, sea turtles, and a rare type of soft coral known as yellow gorgon (Topaloglu, 2016). The study area is placed at the east side of the Island, and the size is 18 m × 90 m. In the study area, the underwater topographic elevations are between −1 m and −5.5 m according to the reference bathymetric model. Figure 1 shows the Istanbul in the Turkey map, location of Tavşan Island in Istanbul, and the study area on RGB orthomosaic of the Island.

The aerial photos of the Tavşan Island were captured with an average ground sampling distance (GSD; i.e., pixel size) of 3.4 cm by using DJI Phantom IV MS UAV. The UAV includes a FC6360 MS camera which have Red, Green, Blue, Red Edge, and NIR monocrome sensors and a traditional RGB sensor for visible light imaging. In addition, the UAV has a real-time kinematic (RTK)

(A) Istanbul in Türkiye map, **(B)** location of Tavşan Island in Istanbul, **(C)** the study area on RGB orthomosaic of the Island.
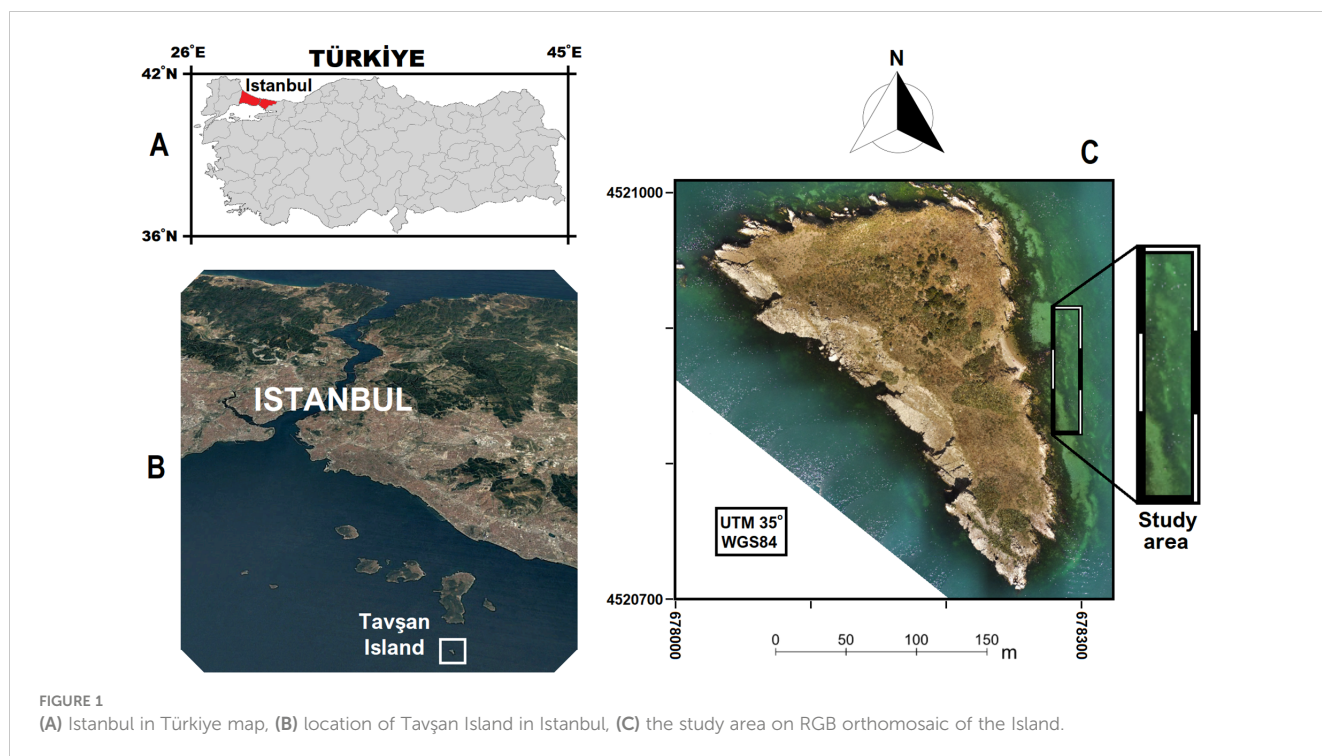
global navigation satellite system (GNSS) receiver for precise positioning. Although the UAV has an RTK receiver, ground control points (GCPs) have been established in the Island against RTK signal interruptions that frequently occur when flying over water surfaces. The GCPs were measured by utilizing a CHC i80 GNSS receiver in fixed positioning mode for the highest positioning accuracy (>3 cm). Since the MS UAV flights took 3 h–4 h, the aerial photos were affected by different lighting due to atmospheric and solar conditions; that is why radiometric calibration, converting the digital number into a unit of scene reflectance, was required (Guo et al., 2019). For radiometric calibration, MAPIR Camera Reflectance Calibration Ground Target Package V2 was employed. Table 1 shows the specifications of the used UAV, GNSS receiver, and radiometric calibration ground target.

3 Methodology

The methodology of the study consists of three main stages: i) UAV data acquisition and photogrammetric processing, ii) generation of UAV DBMs by multiple methods, and iii) accuracy assessment of UAV DBMs. These stages were presented in detail as subsections of Methodology.

3.1 UAV data acquisition and photogrammetric processing

In UAV data acquisition, many parameters should be considered for a safe flight and the generation of high-quality products. One of the most significant parameters is the flying altitude which directly affects the GSD that determines spatial

resolution (Koch et al., 2019). Due to determining of the flying altitude from the UAV home point, the spatial resolution in elevated areas is higher than that of flat topography due to being closer to the UAV camera. The maximum object height in the flying path is another main parameter in flying altitude determination. In the elevated part of the Tavşan Island, two different high masts exist for safety purposes. Regarding these circumstances, two different altitude flights were planned. While the 80-m flying altitude was preferred for elevated parts of the Island, 60 m was applied for low parts and 633 aerial photos with average 3.4 cm GSD were achieved. To obtain maximum shallow water coverage and high-performance 3D modeling, different geometry polygonal flying paths with nadir view were applied in the flights.

The workflow used up to very high-resolution (VHR) orthomosaic generation with acquired MS UAV data is shown in Figure 2. Photogrammetric processing steps were completed utilizing Agisoft Metashape, one of the most preferred UAV data processing software in scientific applications. Similar to popular UAV data processing software such as Pix4D, ContextCapture, and Visual-SfM, Agisoft Metashape uses the low-cost and robust structure from motion (SfM) technique for high-resolution image matching and generation of 3D geometry from a series of overlapping aerial photos (Westoby et al., 2012). One of the main objectives of this study is to determine the effect of different imaging bands on bathymetric model quality; that is why the orthomosaic generation process was applied two times as for RGB single bands and the R, G, B, red edge, and NIR multi-bands separately. In the RGB band workflow, distinct from the MS workflow, radiometric calibration is not included because of single band usage.

For correct validation, raw imagery derived from remote sensing platforms has to be calibrated before scientific analyses (Lee et al., 2004). In this study, the calibration of the aerial photos

TABLE 1 Specifications of used UAV, GNSS receiver, and radiometric calibration ground target.

DJI P4 MS UAV		CHC-i80 GNSS Receiver– GCP - MAPIR	
Specification	**Value**	**Specification**	**Value**
Camera	FC6360, 6 sensors 1/2.9″ CMOS, RGB + 5 Monochrome, 2.08 MP	**GNSS technology**	GPS, GLONASS, GALILEO, BeiDou, SBAS, NavIC
Camera focal length	5.7 mm	**Operating system**	Linux
Gimbal	3-axis, (pitch, roll, yaw) Vertical: −90°–+30°	**Working modes**	Static, VRS RTK, UHF RTK, all surveying modes
RTK GNSS receiver	Include	**Network-RTK**	Available
Positioning accuracy of RTK GNSS	1 cm + 1 ppm H; 1.5 cm + 1 ppm V	**Positioning accuracy RTK**	± 0.8 cm H, ± 1.5 cm V with initialization reliability >99.9%
Hover accuracy range	RTK enabled: ± 0.1 m V, ± 0.1 m H; RTK disabled: ± 0.1 m V, ± 0.3 m H (Vision); ± 0.5 m V, ± 1.5 m H (GPS)	**Battery**	Dual; static up to 10 h, cellular receive only up to 9 h, UHF receive/transmit up to 6 h
Max. flight time/weight	27 min/1487 gr	**Modem—Bluetooth**	4G, 3G, GSM – V4
Max. speed	13.85 m/s	**Internal memory**	32 GB
Max. operational wind speed	10 m/s	**GCP**	0.25 m × 1 m, polycarbonate
Max. operational temperature	0°–40°	**Radiometric reflectance targets**	4 colors: white, light gray, dark gray, black

was completed in two steps as radiometric and geometric. While geometric calibration is sufficient for RGB data, radiometric calibration is additionally mandatory for MS data to achieve more accurate spectral reflectance data (Teixeira et al., 2020). To use in radiometric calibration, before the flights, the photos of MAPIR Camera Reflectance Calibration Ground Target Package V2 were captured by MS UAV. In these photos, four colors placed on MAPIR V2 as white, black, light gray, and dark gray were masked separately to isolate them from the rest for a correct calibration (Sefercik et al., 2023a). The exact spectral reflectance values of these colors were obtained from the distributor of MAPIR. The geometric calibration of the aerial photos was realized in two steps as initial (mutual) alignment and absolute orientation. In initial alignment, aerial photos were matched by applying the SfM approach and sparse point clouds were generated. For absolute orientation, 13 GCPs distributed on the Island before the flight were used. In addition, 16 and 4 tie points were manually marked around the sea surface for RGB and MS data, respectively, to include aerial photos on the sea area to the orientation. The precision of GCPs and additional tie points was determined as RMSE utilizing Equation 1 where $\hat{X}i$, $\hat{Y}i$, $\hat{Z}i$ = estimated values for i camera position and Xi, Yi, Zi = input values for i camera position.
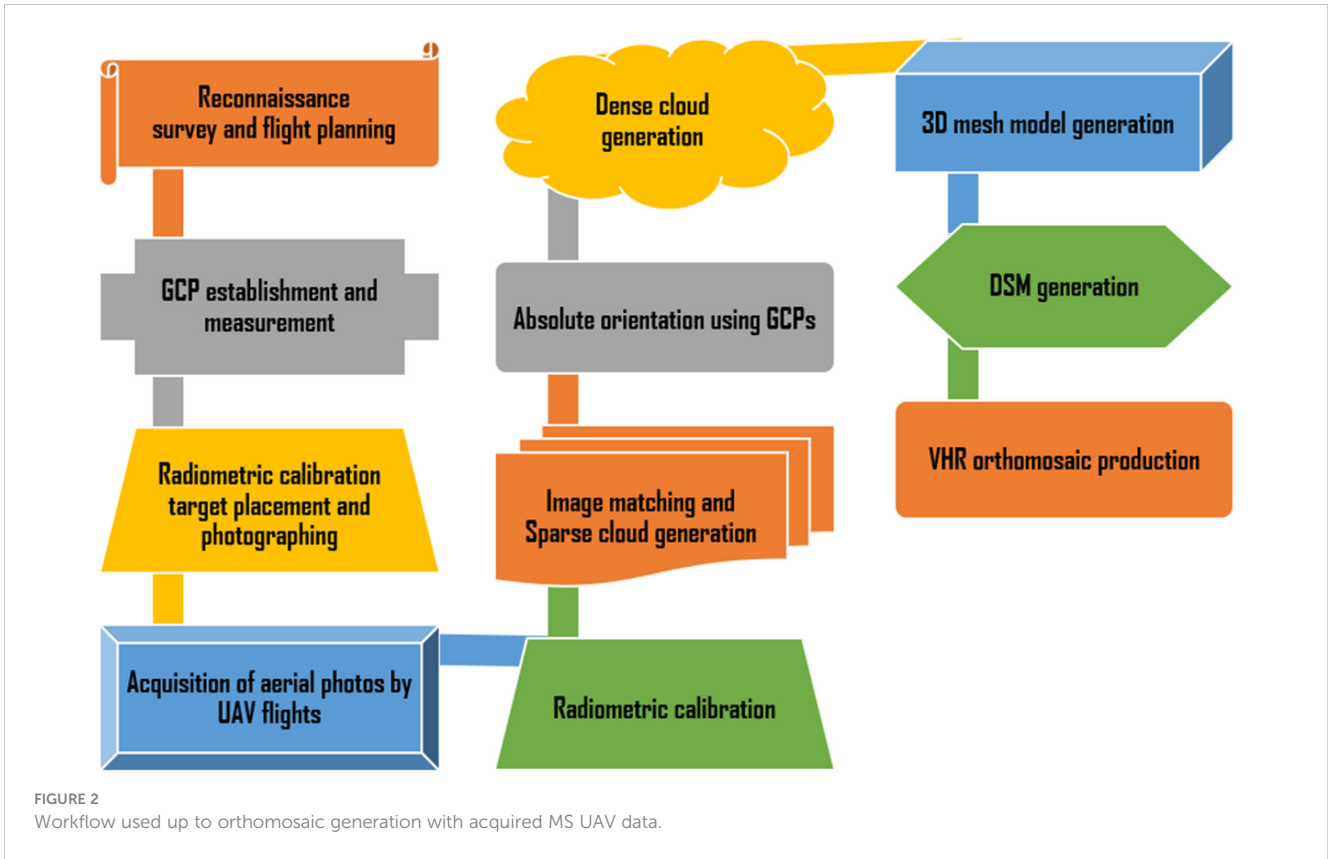
$$RMSE_{GCP}=\sqrt{\frac{\sum_{i=1}^{n}(\hat{X}_i-X_i)^2+(\hat{Y}_i-Y_i)^2+(\hat{Z}_i-Z_i)^2}{n}} \quad (1)$$

The accuracy of the model after absolute orientation was calculated employing 5 of 13 GCPs as independent check points (ICPs). Unlike GCPs, ICPs are not used for absolute orientation and determine the 3D accuracy of the geometrically calibrated model by calculating the difference from reference GNSS measurements (Sefercik and Nazar, 2023b). The accuracies of the models acquired by oriented photos regarding ICPs were calculated by Equations 2–5. Figure 3 illustrates the masked reflectance targets and GCP distribution on the Tavşan Island. RMSE values of GCPs, additional tie points, and ICPs for MS and RGB data geometric calibration are separately presented in Table 2. Table 2 shows that the average RMSE of ICPs is approximately ±5 cm for both MS and RGB models; this means ±1.5 pixels (i.e., 5 cm/3.4 cm) and is quite sufficient considering the steep and irregular topography of the island.

$$RMSE_X=\sqrt{\frac{\sum(X_{ref}-X_{DBM})^2}{n}} \quad (2)$$

$$RMSE_Y=\sqrt{\frac{\sum(Y_{ref}-Y_{DBM})^2}{n}} \quad (3)$$

$$RMSE_Z=\sqrt{\frac{\sum(Z_{ref}-Z_{DBM})^2}{n}} \quad (4)$$

FIGURE 2
Workflow used up to orthomosaic generation with acquired MS UAV data.

$$RMSE_{ICP} = \sqrt{RMSE_X^2 + RMSE_Y^2 + RMSE_Z^2} \qquad (5)$$

Following geometric calibration processes, dense point clouds were generated for RGB and MS data using mild depth filtering, which reduces noisy points while preserving fine details. Depth filtering evaluates pairwise depth maps for matching aerial photos using the component filter, taking into account the pixel ranges from the sensor (Tinkham and Swayze, 2021). In dense point cloud of water-included study areas, when sunlight is reflected from the sea surface at the same angle as the UAV sensor views, sunlight occurs and causes considerable
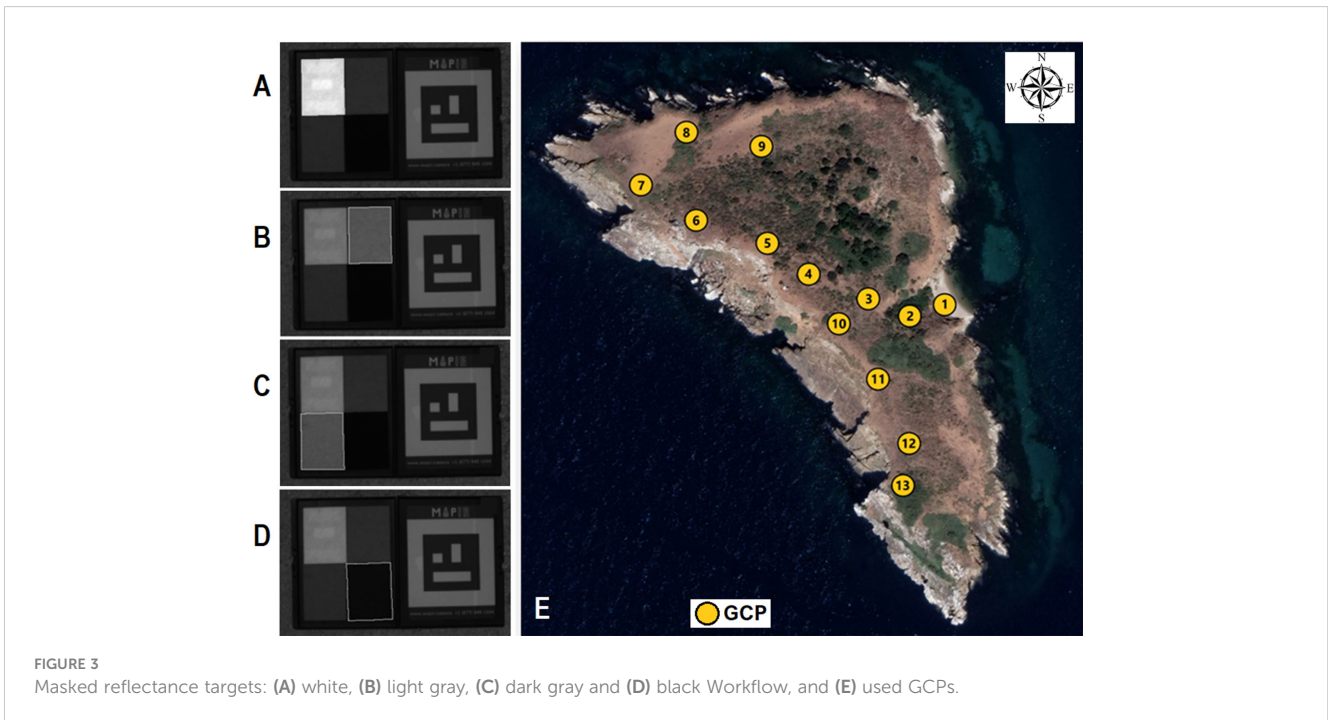

FIGURE 3
Masked reflectance targets: **(A)** white, **(B)** light gray, **(C)** dark gray and **(D)** black Workflow, and **(E)** used GCPs.

TABLE 2   RMSE values of GCPs, additional tie points, and ICPs for MS and RGB data geometric calibration (ICPs are dark).

GCP/TP	RGB			MS		
	RMSE (m)	Average RMSE (m)		RMSE (m)	Average RMSE (m)	
		29 GCPs/TPs	5 CPs		17 GCPs/TPs	5 CPs
GCP-1	0.032/0.088			0.020/0.083		
GCP-2	0.028			0.002		
GCP-3	0.010			0.012		
GCP-4	0.008			0.009		
GCP-5	0.003/0.032			0.006/0.035		
GCP-6	0.012			0.006		
GCP-7	0.010			0.012		
GCP-8	0.005/0.016			0.004/0.013		
GCP-9	0.009			0.005		
GCP-10	0.012/0.042			0.009/0.051		
GCP-11	0.028			0.010		
GCP-12	0.050			0.008		
GCP-13	0.053/0.078			0.021/0.071		
TP-1	0.122					
TP-2	0.066	0.045	**0.058**		0.043	**0.056**
TP-3	0.023					
TP-4	0.007					
TP-5	0.015					
TP-6	0.001					
TP-7	0.004			Not used		
TP-8	0.024					
TP-9	0.022					
TP-10	0.007					
TP-11	0.041					
TP-12	0.083					
TP-13	0.118			0.141		
TP-14	0.010			0.007		
TP-15	0.015			0.020		
TP-16	0.027			0.038		

noise. Additionally, the reduction of image matching quality depending on low correlation of aerial photos in water areas causes noise. Therefore, generated RGB and MS dense point clouds were filtered by fencing and classifying noisy points. For the refraction correction of RGB and MS dense point clouds, an iterative approach proposed by Dietrich (2017), based on the calculation of a set of equations to correct the refraction of point/camera combinations in the point cloud, was used and it is available from a GitHub repository (https://github.com/geojames/pyBathySfM). In this approach, based on Snell's law (Equation 6), which governs the refraction of light between two

different mediums, a set of equations is solved for the actual depth h of the seafloor point.

$$n_1 sini = n_2 sinr \qquad (6)$$

In Equation 6, while the refractive index of seawater n_1 is 1.337 (Harvey et al., 1998) and the refractive index of air n_2 is 1.0, the incidence angle from the seabed to the water surface is i and the refraction angle from the water surface to the optical sensor is r. As light rays pass through the air/water interface, they are refracted according to the Snel/Descartes law of refraction, so as the camera

moves, the i and r angles also fluctuate, affecting the h values (Westaway et al., 2001; Butler et al., 2002). Hence, there is a need to solve Equation 6 for each camera position. This can be simplified to Equation 7, where x represents the horizontal distance from the air/water interface to the underwater point, and h_a is the apparent depth.

$$sin i \cong tan i = \frac{x}{h} \qquad sin r \cong tan r = \frac{x}{h_a} \qquad h = 1.337 \times h_a \qquad (7)$$

The initial step involved selecting all cameras associated with visible points within the study area. The estimated camera positions (x, y, z), orientations (pitch, roll, yaw), and internal parameters (focal length and sensor size) were then used to calculate the instantaneous field of view (IFOV) for each camera. Angles i and r were calculated according to Equation 8 for every visible point within the IFOV. Here, D represents the Euclidean distance ($\sqrt{(X_c - X_a)^2 + (Y_c - Y_a)^2}$) between the optical sensor and the underwater point and dH represents the vertical distance between the optical sensor and the underwater point ($Z_c - Z_a$).

$$r = tan^{-1} = \frac{D}{dH} \qquad i = sin^{-1}(\frac{n_2}{n_1} * sin r) \qquad (8)$$

Estimating a planar water surface is crucial for obtaining water surface elevations WS_z to establish $h_a (h_a = WS_z - Z_a)$. The water depth in the area can be measured, and water edge points can be sampled in the SfM point cloud to achieve this. In both RGB and MS point clouds, water edge points are selected based on the noticeable color shift from wet to dry points. For each combination of point/camera, the calculation of h is carried out using the aforementioned equations and the formula for the x value (Equation 9).

$$x = h_a * tan r \qquad i = \frac{h_a * tan r}{tan[sin^{-1}(\frac{n_2}{n_1} * sin r)]} \qquad (9)$$

Finally, the true Z-coordinate of the underwater point Z_p can be calculated using Equation 10. Since Z_a is a certain value, h_a is also certain for each point, resulting in different x and h values for each camera. As a result, the values of x and Z_p will vary, resulting in the final corrected depth being the average of all h values ($\bar{h}$), explained in Butler et al. (2002) as the depth correction value $h_c (h_c = h - h_a)$ calculated for each camera position and the average of these values

are used to determine the ($\bar{h}$), which is then subtracted from the surface of the water to obtain the corrected height.

$$Z_p = WS_z - \bar{h} \qquad (10)$$

Dense point cloud consists of non-continuous point-based vector form; for more realistic and continuous raster form, it has to be converted into the 3D solid form. That is why, using the refraction-corrected dense point clouds, 3D mesh models and digital surface models (DSMs) were generated and finally 3.42-cm GSD RGB and 3.39-cm GSD MS orthomosaics were produced (Figure 4). To demonstrate the effect of radiometric calibration, MS orthomosaics were presented with and without radiometric calibration separately in Figure 4.

3.2 Generation of UAV DBMs by multiple methods

In the study, four DBMs with different characteristics were generated to evaluate the effect of spectral bands and different principle generation methods on UAV-derived DBM potential in shallow water. While RGB and MS DBMs were generated from 3D dense point clouds derived by RGB and MS calibrated aerial photos, in Stumpf and Lyzenga DBM production, reflectance values of 2D MS orthomosaic were employed. The high-quality RGB and MS DBMs were generated in Surfer software using reprocessed dense point clouds in MicroStation Terrasolid, which presents more detailed point filtering advantage in comparison with Agisoft Metashape. For the generation of DBMs by Stumpf and Lyzenga empirical methods, the following methodologic workflow presented in Figure 5 was applied on MS UAV orthomosaic utilizing the ENVI[TM] 5.6 suite and QGIS 3.23.3 for the determination of model parameters and LibreOffice for error calculations. In preprocessing, the study area was subset and the MS orthomosaic was downsampled to 10-cm grid to generate 10-cm Stumpf and Lyzenga DBMs for 100% pixel-based overlap with the reference DBM and better interpretation with RGB and MS DBMs.

Proper use of water pixels requires masking out any pixel containing land features including soil, vegetation, rocks, and urban. For this purpose, water pixels were extracted from the MS UAV orthomosaic by generating a land mask. This was
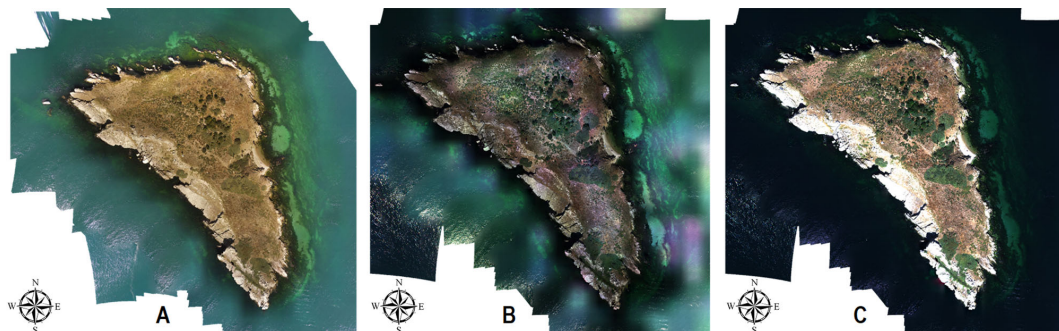

FIGURE 4
Generated Orthomosaics: **(A)** RGB, **(B)** MS without radiometric calibration, **(C)** MS with radiometric calibration.
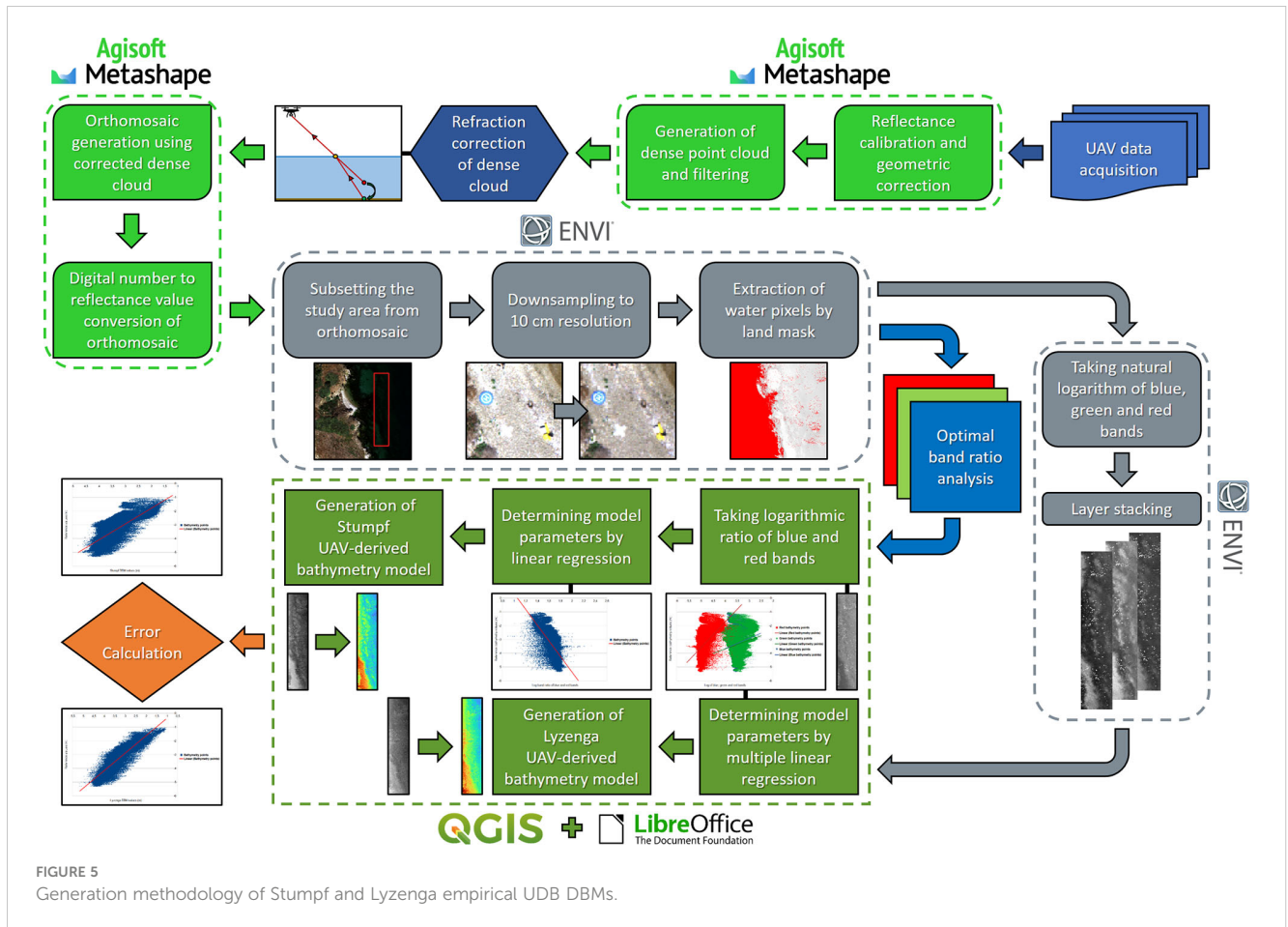
FIGURE 5
Generation methodology of Stumpf and Lyzenga empirical UDB DBMs.

accomplished through the normalized difference water index (NDWI) presented by McFeeters (1996) to delineate features of open water and improve their visibility in remotely sensed imagery by adopting a band ratio of green and NIR bands (Equation 11). This index is created firstly for maximizing the reflectance of water features by means of green wavelength; secondly to minimize the low reflectance values of the NIR band being absorbed mostly by water features; and thirdly to benefit from the high reflectance of vegetation and soil features in NIR band (Xu, 2006). In Equation 11, ρ_Green is the reflectance value of green band pixels and ρ_NIR is the reflectance value of NIR band pixels. Results of NDWI displayed that index values of water features were mostly larger than 0.5 similar to Du et al. (2016). Therefore, this value was selected as a threshold for water–land separability and a land mask was generated.

$$NDWI = \frac{\rho_{Green} - \rho_{NIR}}{\rho_{Green} + \rho_{NIR}} \qquad (11)$$

Indeed, Stumpf and Lyzenga are two different empirical SDB methods which are conventionally applied to satellite imagery in the literature. In this study, we adapted these methods to UAV-derived DBM generation, that is why these models will be called UDB models. An empirical solution was proposed by Stumpf et al. (2003) based on ratio transform for producing SDB models over shallow waters. This solution follows the fundamental that water

absorptivity differentiates from band to band and as the depth increases, the spectral irradiance decreases at a higher rate in the higher absorption band (green band) compared with the lower absorption band (blue band) (El-Sayed, 2018). It uses the natural logarithmic ratio of two different visible bands with dissimilar absorptivities for derivating the depth value over different bottom types, and it can be applied to low-albedo depth features as an alternative to the linear transform approach (Equation 12). In addition, the ratio transform algorithm makes utilization of two bands to reduce the number of depth retrieval parameters and it can minimize errors due to differing variations in the atmosphere, water column, and sea bottom (Pushparaj and Hegde, 2017).

$$Z = m_1 \frac{\ln\left(nR_w(\lambda_i)\right)}{\ln\left(nR_w(\lambda_j)\right)} - m_0 \qquad (12)$$

In the equation, Z is the calculated depth value, m_1 is a changeable constant to scale the ratio to depth, n is a fixed constant for all zones, for the depth of 0 m m_0 is the offset, and whereas $R_w(\lambda_i)$ is the reflectance values of high absorption band $R_w(\lambda_j)$ defines the reflectance values of the low absorption band. However, to properly apply the Stumpf UDB model to MS UAV data, the most suitable band combination should be determined. This was carried out by using optimal band ratio analysis (OBRA), and wavelength pairs that establish the strongest relationship linearly between Z and the remotely sensed variable X were
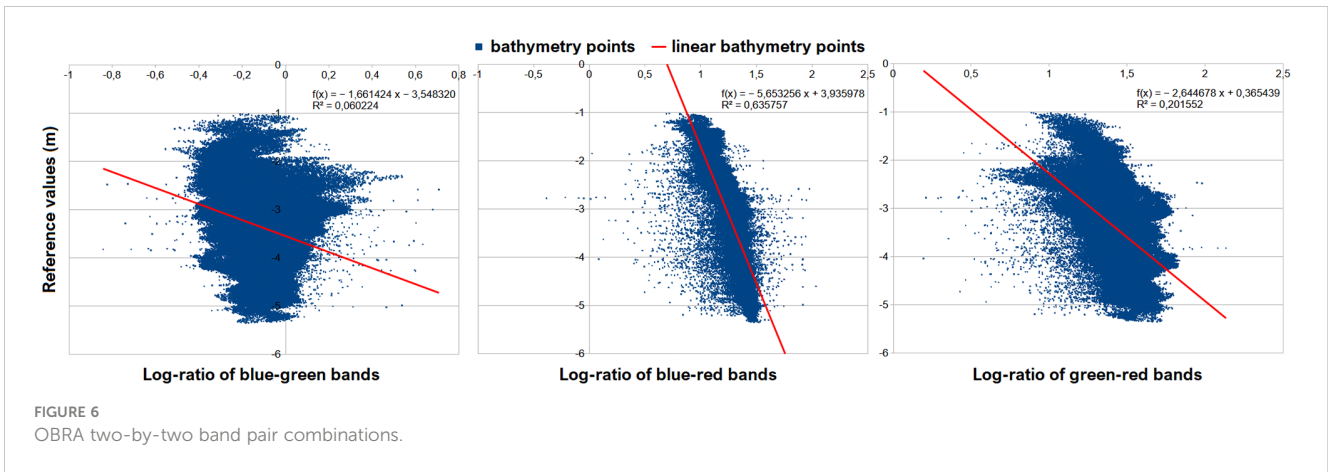
FIGURE 6
OBRA two-by-two band pair combinations.

analyzed (Legleiter et al., 2009). In addition, OBRA utilizes a log-ratio of bands so it aids in the selection of bands that are less sensitive to substrate variability of sea bottom (Dierssen et al., 2003; Niroumand-Jadidi and Vitti, 2016). In Equation 13, X is calculated by applying log-ratio to selected bands $R_w(\lambda_i)$ and $R_w(\lambda_j)$ reflectance values. Two-by-two band pair combinations were evaluated by conducting linear regression between X and flow depth. In this evaluation, single-beam echosounder reference bathymetry values d to be selected as the optimal pair which has the highest correlation coefficient (R^2) (Figure 6).

$$X = ln\left[\frac{R_w(\lambda_i)}{R_w(\lambda_j)}\right] \qquad (13)$$

R^2 values of each two-by-two band pair were obtained as 0.060224, 0.635757, and 0.201552 for blue–green, blue–red, and green–red, respectively. After carrying out OBRA using bands of MS orthomosaic, having the highest R^2 compared with other band combinations λ_i and λ_j were selected as the λ_{Blue} and λ_{Red}, respectively, to establish a log-band ratio. In this step, to ensure that logarithms will be positive in any situation and to eliminate any non-linear response from depth, fixed constant n was selected as 1,000 which is conventionally utilized in literature (Bramante et al., 2013; Caballero and Stumpf, 2020, 2023). The model parameters m_0 and m_1 were determined by applying a linear regression between the logarithmic band ratio and the single-beam echosounder reference bathymetry values as shown in Figure 7 (Zhu et al., 2020). By applying a linear regression, the trend line equation $f(x)$ and R^2 were obtained (Equation 14).

$$f(x) = m_1 \frac{ln\left(nR_w(\lambda_i)\right)}{ln\left(nR_w(\lambda_j)\right)} + m_0 \qquad (14)$$

$$= -5.702447 \frac{ln\left(nR_w(\lambda_i)\right)}{ln\left(nR_w(\lambda_j)\right)} + 6.018247 \quad R^2 = 0.514420$$

As mentioned before, the possibility of generating UDB models from MS aerial photos was further analyzed by adopting another empirical method Lyzenga (1978), based on log-linear inversion of MS bands with advantages of i) enhanced operational flexibility due to spectral bands not restricted to the ones with the same coefficients of water attenuation, ii) enhanced performance in separation of bottom

substances with similar spectral behavior, and iii) utilization of more than two bands in contrast to log-ratio based methods providing increased robustness. This method assumes that the optical properties of a water area are uniform over a sample region and reflectance values obtained from MS bands can be combined to acquire information about water attenuation (Lyzenga, 1981). However, Lyzenga et al. (2006) stated that whereas in some cases the atmospheric scattering and optical properties of water are amply uniform, in general, there may be pixel-to-pixel variations due to sunlight effect, haze, or fluctuations in water quality. The Lyzenga UDB model operates upon the fact that the reflected values from the sea floor can be approximated by using bottom reflectance values to form a linear function and utilizing water depths to produce an exponential function (Equation 15). In other words, single-beam echosounder reference bathymetry values are used to calibrate the parameters of the Lyzenga UDB model to estimate unknown depth values (Figueiredo et al., 2015).

$$Z = m_0 + \sum_{i=1}^{N} m_i ln[L(\lambda_i) - L_\infty(\lambda_i)] \qquad (15)$$

where Z is the calculated depth values in meters, m_0 and m_i are model parameters calculated for N MS bands, and $L(\lambda_i)$ and $L_\infty(\lambda_i)$ are the spectral reflectance and the deep-water reflectance for λ_i MS band, respectively. Model parameters were calculated for ($i = 1,2,3$) spectral bands as blue, green, and red by doing multiple linear regression between logarithmic band values and single-beam echosounder reference bathymetry values (Figure 8). After multiple linear regression, Lyzenga UDB model parameters m_0 and m_i were obtained using Equation 16.

$$f(x) = m_{Blue}x_1 + m_{Green}x_2 + m_{Red}x_3 + m_0$$

$$= -6.469978x_1 + 0.378375x_2 + 5.684873x_3 + 2.477796$$

$$R^2 = 0.639605 \qquad (16)$$

Noise effects, especially those caused by sunlight, on Stumpf and Lyzenga DBMs were filtered using MicroStation Terrasolid software to avoid misleading results in accuracy analyses. Figure 9 shows the linear regression results of Stumpf and Lyzenga DBM values after

Linear regression between the log-band ratio and the reference values for determination of the model parameters m_0 and m_1.
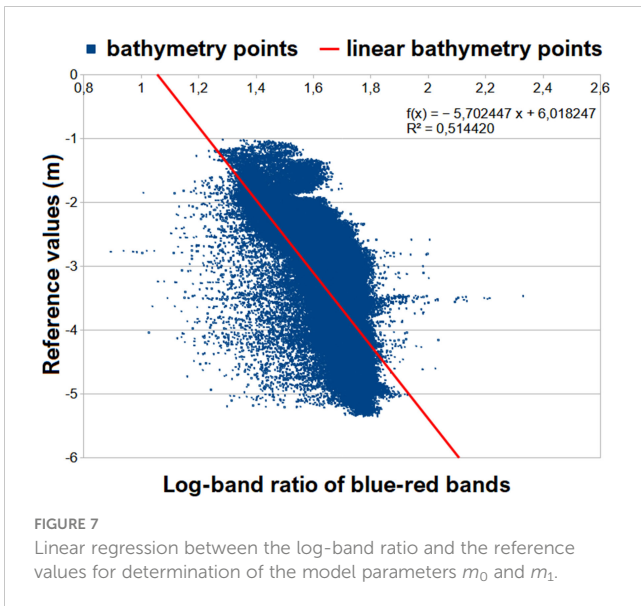
final filtering. Considering Figure 9, it can be mentioned that Lyzenga DBM estimates the depth values better than Stumpf DBM. The R^2 value is calculated as 0.814660 for Lyzenga whereas 0.612081 for Stumpf, which demonstrates that in-depth estimation via UDB adopting more than spectral bands can improve the performance in comparison with band ratio approach.

3.3 Accuracy assessment of UAV DBMs

Accuracy of DBMs is assessed with two common approaches as point-based and model-based similar to other digital 3D models like digital surface, elevation, terrain, and canopy height models. While the point-based approach uses limited number of control points distributed on the study area, the model-based approach utilizes reference models. The advantage of the model-based approach is that it enables all pixels of the DBM to participate in the accuracy

evaluation by comparing matching pixels in the reference 3D model (Lin et al., 1994). In this study, the model-based approach was adopted by using a reference DBM derived from single-beam echosounder measurements and all pixels of the generated DBMs were included in the accuracy analyses. In reference data acquisition, a Navisound NS 600 RT-1 single-beam echosounder, equipped with a two-channel 50-kHz transducer and a GNSS receiver, was employed. The device can reach the depth of 600 m with 1° beam width (Celik et al., 2023). As known, sonar ships generally cannot safely navigate in shallow areas. Considering this situation, a small boat, which could easily approach the island shores, was used for single-beam sonar data collection. Both the year of UAV flights and the reference single-beam echosounder data collection is 2023.

In the accuracy assessment of generated DBMs, comprehensive visual and statistical approaches were performed. In visual approaches, DBMs, and the differential DBMs (DIFFDBM) (Equation 17) which are the height error maps between generated DBMs and the reference DBM, were generated by utilizing Surfer and LISA software and interpreted. In statistical approaches, the accuracies of the generated DBMs were calculated using the standard deviation (SZ) of the height differences between the DBMs and the reference model, as well as the normalized median absolute deviation (NMAD), obtained by normalization of the median absolute deviation (Equations 18–20). The linear errors with 90% or 95% probability levels (LE90 and LE95, respectively) were not preferred as accuracy metrics because they are strongly depending on the percentage of blunders and they do not match with the frequency distribution of the height differences in most cases (Sefercik et al., 2013; Jacobsen, 2014). The statistical analyses were completed utilizing BLUH software from Leibniz University Hannover.

$$DIFFDBM = DBM_{Generated} - DBM_{Ref} \quad (17)$$

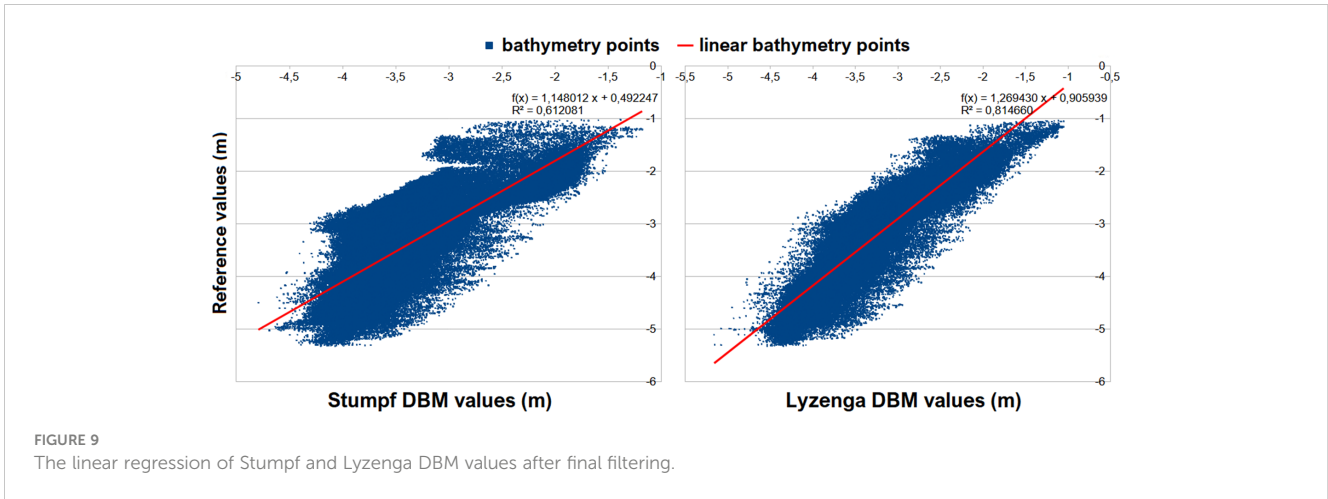$$SZ = \sqrt{\frac{\sum_{i=1}^{n}(\Delta Z_i - \mu)^2}{n-1}} \quad (18)$$

Multiple linear regression between the logarithmic band values and the reference values for determination of the model parameters m_0 and m_i.
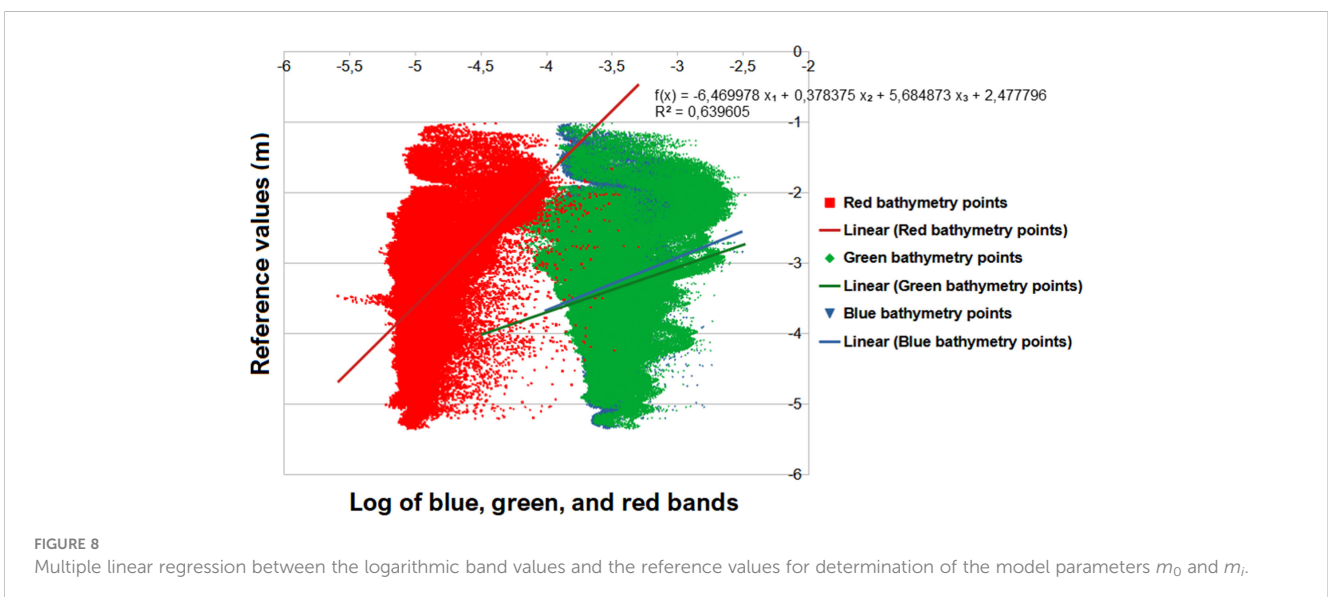
FIGURE 9
The linear regression of Stumpf and Lyzenga DBM values after final filtering.

$$MAD=\tilde{x}_i\left[\left|\Delta Z_i-\tilde{x}_j(Z_j)\right|\right] \qquad (19)$$

$$NMAD=1.4826*(MAD) \qquad (20)$$

where n is the total pixel number of generated DBMs; ΔZ is the height differences from reference DBM and μ is the arithmetic mean of the ΔZ (bias). $\tilde{x}_j$ is the median of ΔZ univariate dataset (ΔZ_1, ΔZ_2, ΔZ_3, ..., ΔZ_n) and $\tilde{x}_i$ is the median of absolute values of the ΔZ dataset from $\tilde{x}_j$. In normal ΔZ distribution, the values of SZ and NMAD are expected as similar. However, a qualified 3D model generation with optical remote sensing in underwater conditions is not as simple as surface conditions and in many cases large outliers are likely to arise. In that case, NMAD is used as a robust scale estimator to estimate the scale of the ΔZ distribution and can be considered as an estimate for the standard deviation more resilient to outliers in the dataset (Höhle and Höhle, 2009).

To estimate the relative accuracy level between neighboring pixels on produced DBMs, contour maps of the evaluated DBMs were created and relative standard deviation (RSZ) was calculated for each pixel using 10 pixel diameter (point spacing × 10) distance groups (D) by Equation 21. In the equation, D_l and D_u are the lower and upper ranges of the group and DZ_i and DZ_j are closely neighbored pixels. For each pixel in distance group, the height difference from the reference DBM is considered. In Equation 21, n_v is the number of point combinations in the distance group. To normalize RSZ to SZ, a multiplication factor of 2 for n_v was employed. If the height differences of the neighbored points are independent as a result of error propagation, the RSZ would be the square root of 2.0 larger than SZ, described by $2 \times n_v$.

$$RSZ=\sqrt{\frac{\sum(DZ_i-DZ_j)^2}{2\times n_v}} \quad , \quad D_l < D < D_u \qquad (21)$$

To consider at the interpretations of visual and statistical approaches, Secchi Disc measurements (Zielinski, 2021) were completed around the study area and turbidity depth of the water was determined as 7.4 m. In addition, geoid undulation in the study area was calculated and applied as 36.501 m in the analyses.

4 Results and discussion

As aforementioned, four different DBMs as RGB, MS, Stumpf, and Lyzenga were generated and comprehensively evaluated by visual and statistical approaches utilizing a reference DBM produced from single-beam echosounder data. Figure 10 shows the generated reference DBM and four evaluated DBMs of the study area. According to the reference DBM, the elevation of deep topography is maximum and minimum in the Southwestern and Northeastern sides of the study area, respectively and around −1 m to −5.5 m. In the first view, the bathymetric surface descriptions of RGB and MS DBMs are closer to the reference than Stumpf and Lyzenga DBMs. In fact, the height scale of the MS DBM produced from five-band aerial photos is almost in the same range as the reference. However, the minimum elevation of RGB DBM is around −4.8 m whereas the reference is around −5.5 m. This shows that the limitations of RGB DBM increase as water depth increases. A similar situation exists for Stumpf DBM, which could not identify topographic details lower than ∼−4.8 m.

The model-based absolute vertical accuracy assessment results of the generated DBMs are presented in Table 3. The systematic bias values were calculated and eliminated before the assessment, and SZ and NMAD values do not include bias. The systematic biases were determined as −0.09 m and 0.07 m for RGB and MS DBMs, respectively. As can be seen in Table 3, while the accuracies of RGB and MS DBMs based on SZ and NMAD are around ±0.23–0.27 m, they are around ±0.40–0.55 m for Stumpf and Lyzenga DBMs. This result demonstrates that generation of DBMs directly from 3D dense point clouds of the aerial photos is more reasonable than generation of DBMs using the reflectance values of the MS UAV orthomosaic. In parallel with R^2 values, the accuracy of Lyzenga DBM is higher than Stumpf DBM as both SZ and NMAD. This result also reveals that in-depth estimation via UDB adopting more than spectral bands can improve the performance in comparison with the band ratio approach.

The frequency distribution, SZ, and NMAD of height differences between generated DBMs and the reference DBM is
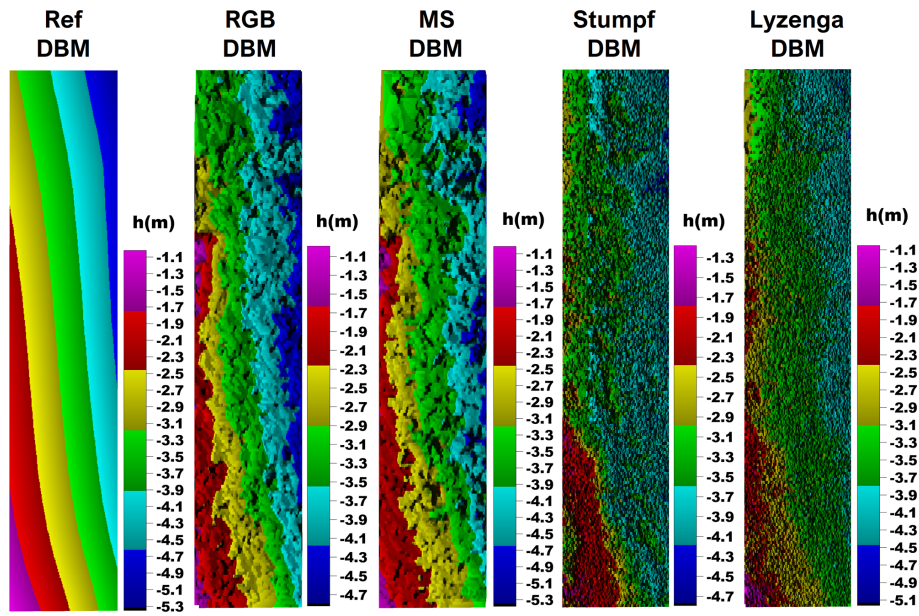
FIGURE 10
Generated RGB, MS, Stumpf, and Lyzenga DBMs.

given by distribution graphics in Figure 11. In the graphic, while the peaks of frequency distribution of height differences (FDZ) of 3D dense point cloud-based RGB and MS UAV DBMs are around 30K pixels, it is around 15K pixels for UDB DBMs. In SZ and NMAD sides, symmetric distribution, which reveals a normal error propagation, is available for all DBMs. The NMAD distributions of RGB and MS DBMs are very similar to each other whereas SZ is slightly different. SZ and NMAD distributions prove that Lyzenga DBM performs better compared with Stumpf DBM.

Figure 12 shows the contour maps which enable to interpret relative vertical accuracies between neighboring pixels on generated DBMs. While the contour lines are clearly detectable in RGB and MS DBMs, small contour islands stand out in UDB DBMs with a discontinuous structure. This points out irregular morphologic description of the seabed. The RSZ values in Figure 13 can assist to interpret this situation. While the RSZ values of RGB and MS DBMs begin around ±0.03 m, they are around ±0.11 m for Stumpf and Lyzenga DBMs. Particularly in Stumpf DBM, the RSZ trend is sharper than expected and the values reach up to ±0.3 m. The main reason of this result may be very high resolution (0.1 m) of the UAV

dataset against space-borne datasets that are commonly utilized for Stumpf and Lyzenga methods.

The DIFFDBMs, differential DBMs of evaluated DBMs with the reference DBM, are presented in Figure 14. For better interpretation, the 3D dense point cloud-based RGB and MS DIFFDBMs and Stumpf and Lyzenga UDB DIFFDBMs were validated separately and the height differences between these validated DBMs and the reference DBMs were classified as between ±1 m, ± 0.5 m, and ±0.1 m. The dark-blue color points out that the height difference interval is exceeded. As mentioned before, water deepens from Southwest to Northeast of the study area and the first result of DIFFDBMs is that the accuracy of all analyzed DBMs decreases with increasing water depth. According to the reference DBM, the depth of the water in the study area is around −1 m and −5.5 m and considering the Secchi disc value (7.4 m), turbidity does not exist. From this point of view, it can be discussed that there is a quality limitation in all four UAV-based DBMs, although there is no turbidity in the study area. In general view, the 3D dense point cloud-based RGB and MS DBMs are more coherent with the reference and in the large part of the ±1-m DIFFDBMs,

TABLE 3 Absolute vertical accuracies of UAV DBMs.

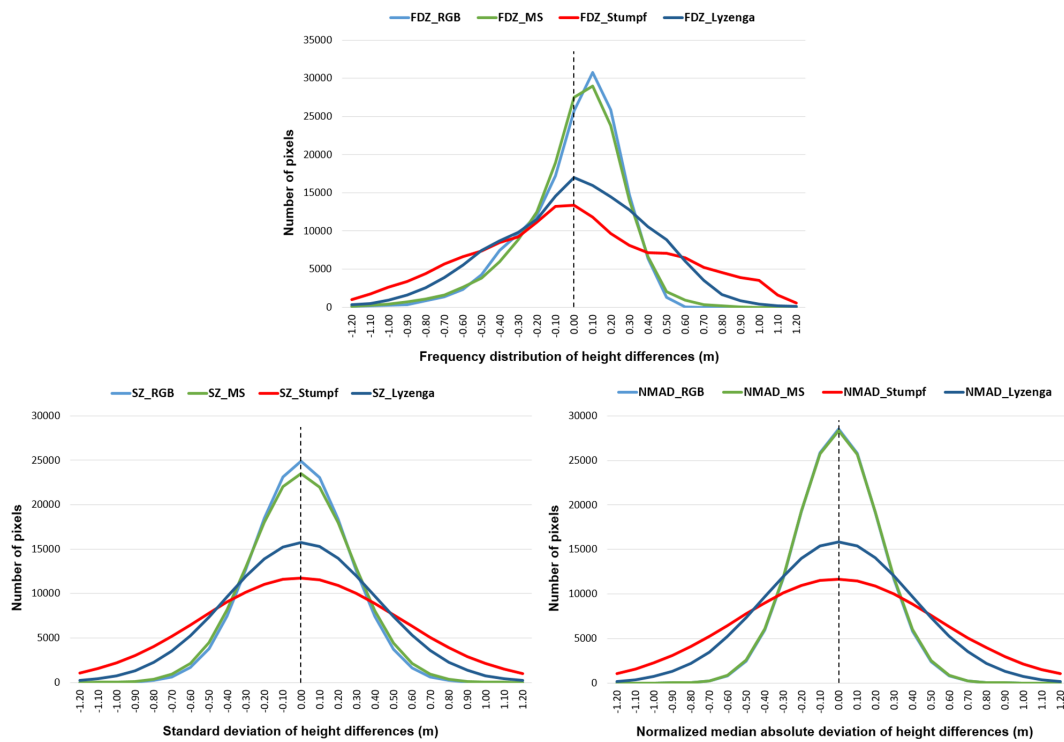| Reference DBM	Evaluated DBM	Eliminated bias (m)	SZ (m)	NMAD (m)
Echosounder single-beam (0.1 m)	RGB (0.1 m)	-0.09	0.26	0.23
	MS (0.1 m)	0.07	0.27	0.23
	Stumpf (0.1 m)	0.00	0.54	0.55
	Lyzenga (0.1 m)	0.00	0.41	0.40

FIGURE 11
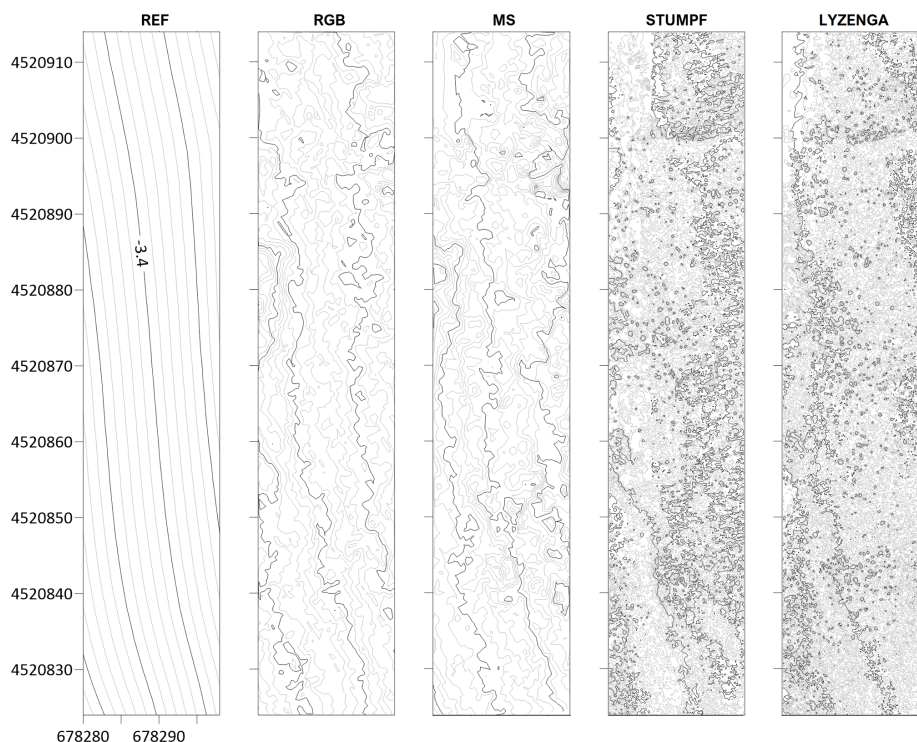FDZ, SZ, and NMAD of DBM height differences from reference DBM.

FIGURE 12
Morphologic structure of generated DBMs.

continuous structure is available without exceeding the height difference scale. There are gaps at the scales of ±0.5 m and ±0.1 m, as expected under underwater conditions.

At the ±0.1-m scale, a considerable part of MS DBM was still coherent with the reference in the deepest areas whereas RGB not. No doubt, this result demonstrates the advantage of multiband usage in UAV-based bathymetric modeling. In the UDB DBM side, it is clearly seen that Lyzenga DBM's compatibility with the reference is much higher than Stumpf DBM in every height difference range. Additionally, the ±1-m scale DIFFDBMs of RGB-MS and Stumpf-Lyzenga DBMs are also included in Figure 14. While the consistency of RGB and MS DBMs is high at minimum and medium depths, differences of close to 1 m occur at maximum depths. Stumpf and Lyzenga DIFFDBM have an irregular distribution of height differences, and considerable differences are noticeable even at minimum depths in addition to deepest areas.

5 Conclusion

The use of UAVs in DBM generation in shallow waters is increasing permanently due to its potential to provide rapid, periodic, and very high-resolution data. However, several parameters related with sensor characteristics, imaging geometry, and calibration requirements limit the UAV-derived DBM quality. In this paper, four DBMs, two from single-band RGB and five-band MS 3D dense point clouds and Stumpf and Lyzenga UDB methods, were generated and comprehensively analyzed by visual and statistical model-based comparison approaches. Before the analyses, radiometric and geometric calibrations of UAV aerial photos were carefully completed. While 13 GCPs and 16 additional TPs were used for absolute orientation of RGB aerial photos, 13 GCPs and 4 TPs were used for MS. In both models, five similar ICPs

selected from GCPs were employed and approx. ± 0.05-m general orientation accuracy were achieved. In optimal MS band combination determination to properly apply Stumpf and Lyzenga UDB models using very high-resolution MS orthomosaic, OBRA were applied and blue–red band combination was preferred accordingly. To avoid misleading depth description, refraction correction was applied in the generation of all evaluated DBMs.

While DBMs and the DIFFDBMs were generated for visual accuracy analyses, SZ and NMAD of the height differences between the DBMs and the reference model were utilized in statistical analyses. In addition to absolute vertical accuracies, the relative accuracies of the DBMs were also exposed by RSZ calculation for neighboring pixels by distance grouping and morphologic analyses by creating contour-lines. The results of visual and statistical analyses demonstrated that i) the accuracy of all analyzed DBMs decreases as water depth increases considering the DIFFDBMs and ii) the accuracy of RGB and MS DBMs produced from 3D point clouds of aerial photos is higher than DBMs produced from Stumpf and Lyzenga UDB methods. While SZ and NMAD of RGB and MS DBMs are around ±0.23 m–0.27 m, this is around ±0.40 m–0.55 m for UDB DBMs. In detailed view, the representation capability of MS DBM is higher than that of RGB DBM and that of Lyzenga DBM is higher than that of Stumpf as the water depth increases. In contrast, it has been observed that the situation reverses in minimum depths. In addition, the systematic bias determined in RGB DBM between reference DBM was determined as −0.09 m, whereas in MS, it was determined as 0.07 m. iii) Relative accuracies of RGB and MS DBMs produced from 3D point clouds are also higher than UDB DBMs. While RSZ values are between ±0.03 m and 0.15 m for RGB and MS DBMs, they are ±0.11–0.30 m for Stumpf and Lyzenga DBMs. In addition, generated contour lines revealed the noisy structure of Stumpf and Lyzenga DBMs in comparison
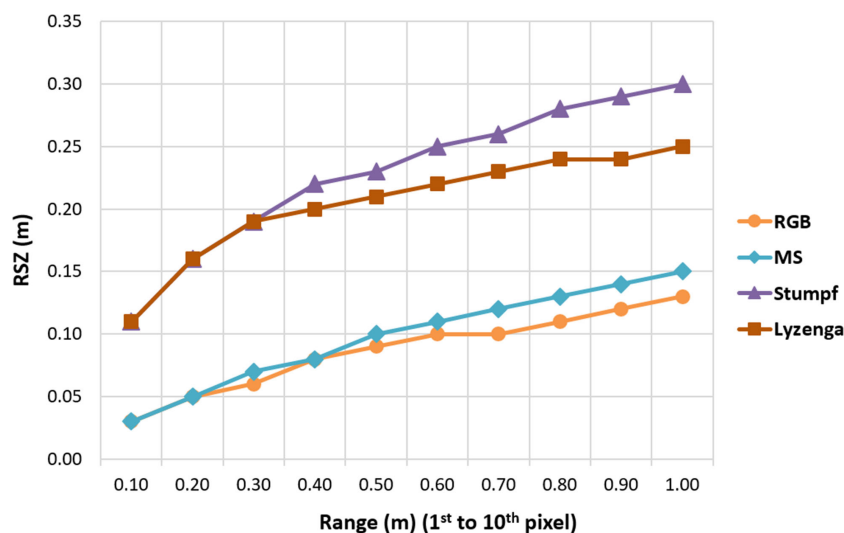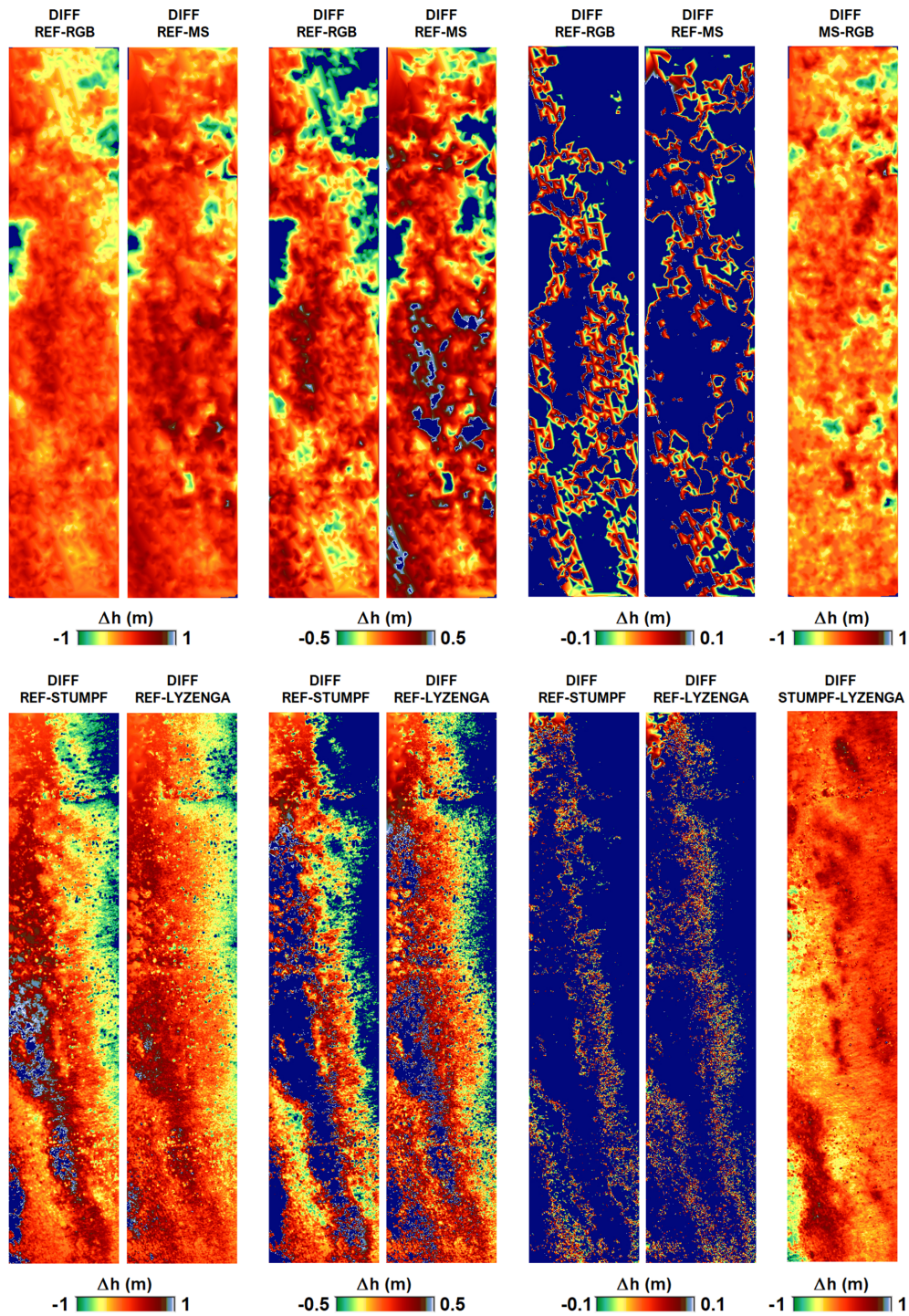

FIGURE 13
RSZ of generated DBMs.

FIGURE 14
DIFF models of RGB, MS, Stumpf, and Lyzenga DBMs according to reference DBM.

with RGB and MS DBMs that cause small contour islands. The reason of this result may be the very high resolution (0.1 m) of the UAV dataset against space-borne datasets that are commonly utilized for Stumpf and Lyzenga methods.

Overall, the accuracy of DBMs generated with different techniques has been documented, thus allowing their use for different bathymetric

purposes to be evaluated. The advantages and disadvantages of generated DBMs compared with each other are discussed. The common conclusion is that the results given by the examined DBMs can be evaluated for shallow waters up to 5-m depth. It has been documented that at depths greater than 5 m, height differences (i.e., height error) between tested and reference DBMs are partially greater than ±1 m.

Data availability statement

The raw data supporting the conclusions of this article will be made available by the authors, without undue reservation. All data used in this study is available in Gebze Technical University, Department of Geomatics Engineering and Istanbul University, Institute of Marine Science and Management.

Author contributions

Funding

Acknowledgments

Conflict of interest

The authors declare that the research was conducted in the absence of any commercial or financial relationships that could be construed as a potential conflict of interest.

Publisher's note

All claims expressed in this article are solely those of the authors and do not necessarily represent those of their affiliated organizations, or those of the publisher, the editors and the reviewers. Any product that may be evaluated in this article, or claim that may be made by its manufacturer, is not guaranteed or endorsed by the publisher.

References

Agrafiotis, P., Karantzalos, K., Georgopoulos, A., and Skarlatos, D. (2020). Correcting image refraction: Towards accurate aerial image-based bathymetry mapping in shallow waters. *Remote Sens.* 12, 322. doi: 10.3390/rs12020322

Agrafiotis, P., Karantzalos, K., Georgopoulos, A., and Skarlatos, D. (2021). Learning from synthetic data: Enhancing refraction correction accuracy for airborne image-based bathymetric mapping of shallow coastal waters. *PFG–Journal Photogrammetry Remote Sens. Geoinformation Sci.* 89, 91–109. doi: 10.1007/s41064-021-00144-1

Agrafiotis, P., Skarlatos, D., Forbes, T., Poullis, C., Skamantzari, M., and Georgopoulos, A. (2018). Underwater photogrammetry in very shallow waters: main challenges and caustics effect removal. *Int. Arch. Photogrammetry Remote Sens. Spatial Inf. Sci.* 42, 15–22. doi: 10.5194/isprs-archives-XLII-2-15-2018

Agrafiotis, P., Skarlatos, D., Georgopoulos, A., and Karantzalos, K. (2019). DepthLearn: learning to correct the refraction on point clouds derived from aerial imagery for accurate dense shallow water bathymetry based on SVMs-fusion with LiDAR point clouds. *Remote Sens.* 11, 2225. doi: 10.3390/rs11192225

Alevizos, E., and Alexakis, D. D. (2022a). Evaluation of radiometric calibration of drone-based imagery for improving shallow bathymetry retrieval. *Remote Sens. Lett.* 13, 311–321. doi: 10.1080/2150704X.2022.2030068

Alevizos, E., and Alexakis, D. D. (2022b). Monitoring short-term morphobathymetric change of nearshore seafloor using drone-based multispectral imagery. *Remote Sens.* 14, 6035. doi: 10.3390/rs14236035

Alevizos, E., Nicodemou, V. C., Makris, A., Oikonomidis, I., Roussos, A., and Alexakis, D. D. (2022a). Integration of photogrammetric and spectral techniques for advanced drone-based bathymetry retrieval using a deep learning approach. *Remote Sens.* 14, 4160. doi: 10.3390/rs14174160

Alevizos, E., Oikonomou, D., Argyriou, A. V., and Alexakis, D. D. (2022b). Fusion of drone-based RGB and multi-spectral imagery for shallow water bathymetry inversion. *Remote Sens.* 14, 1127. doi: 10.3390/rs14051127

Alvarez, L. V., Moreno, H. A., Segales, A. R., Pham, T. G., Pillar-Little, E. A., and Chilson, P. B. (2018). Merging unmanned aerial systems (UAS) imagery and echo soundings with an adaptive sampling technique for bathymetric surveys. *Remote Sens.* 10, 1362. doi: 10.3390/rs10091362

Apicella, L., De Martino, M., Ferrando, I., Quarati, A., and Federici, B. (2023). Deriving coastal shallow bathymetry from Sentinel 2-, Aircraft-and UAV-derived orthophotos: A case study in Ligurian Marinas. *J. Mar. Sci. Eng.* 11, 671. doi: 10.3390/jmse11030671

Belcore, E., and Di Pietra, V. (2022). Laying the foundation for an artificial neural network for photogrammetric riverine bathymetry. *Int. Arch. Photogrammetry Remote Sens. Spatial Inf. Sci.* 48, 51–58. doi: 10.5194/isprs-archives-XLVIII-4-W1-2022-51-2022

Bindoff, N. L., Willebrand, J., Artale, V., Cazenave, A., Gregory, J. M., Gulev, S., et al. (2007). "Observations: Oceanic climate change and sea level, in Climate Change 2007: The Physical Science Basis," in *Contribution of Working Group I to the Fourth Assessment Report of the Intergovernmental Panel on Climate Change*. Eds. S. Solomon, D. Qin, M. Manning, Z. Chen, M. Marquis, K. B. Averyt, M. Tignor and H. L. Miller (Cambridge University Press, Cambridge), 385–428.

Bio, A., Bastos, L., Granja, H., Henriques, R., Madeira, S., and Rodrigues, D. (2015). Methods for coastal monitoring and erosion risk assessment: two. *Portuguese Case Stud.* 15, 47–63. doi: 10.5894/rgci490

Bramante, J. F., Raju, D. K., and Sin, T. M. (2013). Multispectral derivation of bathymetry in Singapore's shallow, turbid waters. *Int. J. Remote Sens.* 34, 2070–2088. doi: 10.1080/01431161.2012.734934

Butler, J., Lane, S., Chandler, J., and Porfiri, E. (2002). Through-water close range digital photogrammetry in flume and field environments. *Photogrammetric Rec.* 17, 419–439. doi: 10.1111/0031-868X.00196

Caballero, I., and Stumpf, R. P. (2020). Towards routine mapping of shallow bathymetry in environments with variable turbidity: Contribution of Sentinel-2A/B satellites mission. *Remote Sens.* 12, 451. doi: 10.3390/rs12030451

Caballero, I., and Stumpf, R. P. (2023). Confronting turbidity, the major challenge for satellite-derived coastal bathymetry. *Sci. Total Environ.* 870, 161898. doi: 10.1016/j.scitotenv.2023.161898

Cai, X., Wu, L., Li, Y., Lei, S., Xu, J., Lyu, H., et al. (2023). Remote sensing identification of urban water pollution source types using hyperspectral data. *J. Hazardous Materials* 459, 132080. doi: 10.1016/j.jhazmat.2023.132080

Cao, B., Fang, Y., Jiang, Z., Gao, L., and Hu, H. (2019). Shallow water bathymetry from WorldView-2 stereo imagery using two-media photogrammetry. *Eur. J. Remote Sens.* 52, 506–521. doi: 10.1080/22797254.2019.1658542

Carbonneau, P. E., and Dietrich, J. T. (2016). Cost-effective non-metric photogrammetry from consumer-grade sUAS: implications for direct georeferencing of structure from motion photogrammetry. *Earth surface processes landforms* 42, 473–486. doi: 10.1002/esp.4012

Casella, E., Lewin, P., Ghilardi, M., Rovere, A., and Bejarano, S. (2022). Assessing the relative accuracy of coral heights reconstructed from drones and structure from motion photogrammetry on coral reefs. *Coral Reefs* 41, 869–875. doi: 10.1007/s00338-022-02244-9

Celik, O. I., Büyüksalih, G., and Gazioglu, C. (2023). Improving the accuracy of satellite-derived bathymetry using multi-layer perceptron and random forest regression methods: A case study of Tavşan Island. *J. Mar. Sci. Eng.* 11, 2090. doi: 10.3390/jmse11112090

Celik, O. I., and Gazioglu, C. (2022). Coast type based accuracy assessment for coastline extraction from satellite image with machine learning classifiers. *Egyptian J. Remote Sens. Space Sci.* 25, 289–299. doi: 10.1016/j.ejrs.2022.01.010

Colkesen, I., Kavzoglu, T., Sefercik, U. G., and Ozturk, M. Y. (2023). Automated mucilage extraction index (AMEI): A novel spectral water index for identifying marine mucilage formations from Sentinel-2 imagery. *Int. J. Remote Sens.* 44, 105–141. doi: 10.1080/01431161.2022.2158049

De Kerf, T., Gladines, J., Sels, S., and Vanlanduit, S. (2020). Oil spill detection using machine learning and infrared images. *Remote Sens.* 12, 4090. doi: 10.3390/rs12244090

Dierssen, H. M., Zimmerman, R. C., Leathers, R. A., Downes, T. V., and Davis, C. O. (2003). Ocean color remote sensing of seagrass and bathymetry in the Bahamas Banks by high-resolution airborne imagery. *Limnol. Oceanogr.* 48, 444–455. doi: 10.4319/lo.2003.48.1_part_2.0444

Dietrich, J. T. (2017). Bathymetric structure-from-motion: Extracting shallow stream bathymetry from multi-view stereo photogrammetry. *Earth Surface Processes Landforms* 42, 355–364. doi: 10.1002/esp.4060

Doukari, M., Katsanevakis, S., Soulakellis, N., and Topouzelis, K. (2021). The effect of environmental conditions on the quality of UAS orthophoto-maps in the coastal environment. *ISPRS Int. J. Geo-Information* 10, 18. doi: 10.3390/ijgi10010018

Dronkers, J. (2005). *Dynamics of Coastal Systems. Advanced Series on Ocean Engineering* Vol. 25 (Hackensack: World Scientific Publishing Company), 519. doi: 10.1142/ASOE

Du, Y., Zhang, Y., Ling, F., Wang, Q., Li, W., and Li, X. (2016). Water bodies' mapping from Sentinel-2 imagery with modified normalized difference water index at 10-m spatial resolution produced by sharpening the SWIR band. *Remote Sens.* 8, 354. doi: 10.3390/rs8040354

El-Sayed, M. S. (2018). Comparative study of satellite images performance in mapping lake bathymetry: Case study of Al-Manzala Lake, Egypt. *Am. J. Geographic Inf. System* 7, 82–87. doi: 10.5923/j.ajgis.20180703.02

Figueiredo, I. N., Pinto, L., and Goncalves, G. (2015). A modified Lyzenga's model for multispectral bathymetry using Tikhonov regulariza-tion. *IEEE Geosci. Remote Sens. Lett.* 13, 53–57. doi: 10.1109/LGRS.2015.2496401

Gao, B. C., Montes, M. J., Li, R. R., Dierssen, H. M., and Davis, C. O. (2007). An atmospheric correction algorithm for remote sensing of bright coastal waters using MODIS land and ocean channels in the solar spectral region. *IEEE Trans. Geosci. Remote Sens.* 45, 1835–1843. doi: 10.1109/TGRS.2007.895949

Guo, Y., Senthilnath, J., Wu, W., Zhang, X., Zeng, Z., and Huang, H. (2019). Radiometric calibration for multispectral camera of different imaging conditions mounted on a UAV platform. *Sustainability* 11, 978. doi: 10.3390/su11040978

Halpern, B. S., Walbridge, S., Selkoe, K. A., Kappel, C. V., Micheli, F., d'Agrosa, C., et al. (2008). A global map of human impact on marine ecosystems. *Science* 319, 948–952. doi: 10.1126/science.1149345

Harris, W. D., and Umbach, M. J. (1972). Underwater mapping. *Photogrammetric Eng.* 38, 765–772.

Harvey, A. H., Gallagher, J. S., and Sengers, J. L. (1998). Revised formulation for the refractive index of water and steam as a function of wavelength, temperature and density. *J. Phys. Chem. Ref. Data* 27, 761–774. doi: 10.1063/1.556029

He, J., Lin, J., and Liao, X. (2022). Fully-covered bathymetry of clear tufa lakes using UAV-acquired overlapping images and neural networks. *J. Hydrol.* 615, 128666. doi: 10.1016/j.jhydrol.2022.128666

Höhle, J., and Höhle, M. (2009). Accuracy assessment of digital elevation models by means of robust statistical methods. *ISPRS J. Photogrammetry Remote Sens.* 64, 398–406. doi: 10.1016/j.isprsjprs.2009.02.003

Isgró, M. A., Basallote, M. D., and Barbero, L. (2022). Unmanned aerial system-based multispectral water quality monitoring in the Iberian Pyrite Belt (SW Spain). *Mine Water Environ.* 41, 30–41. doi: 10.1007/s10230-021-00837-4

Jacobsen, K. (2014). Development of large area covering height model. *Int. Arch. Photogrammetry Remote Sens. Spatial Inf. Sci. XL-4* 40, 105–110. doi: 10.5194/isprsarchives-XL-4-105-2014

Jagalingam, P., Akshaya, B. J., and Hegde, A. V. (2015). Bathymetry mapping using Landsat 8 satellite imagery. *Proc. Eng.* 116, 560–566. doi: 10.1016/j.proeng.2015.08.326

James, M. R., and Robson, S. (2014). Mitigating systematic error in topographic models derived from UAV and ground-based image networks. *Earth Surface Processes Landforms* 39, 1413–1420. doi: 10.1002/esp.3609

Jégat, V., Pe'eri, S., Freire, R., Klemm, A., and Nyberg, J. (2016). "Satellite-derived bathymetry: Performance and production," in *Proceedings of the Canadian Hydrographic Conference* Halifax, NS, Canada. 16–19.

Kavzoglu, T., Colkesen, I., Sefercik, U. G., and Ozturk, M. Y. (2021). Detection and analysis of marine mucilage bloom in the Sea of Marmara by a machine learning algorithm from multi-temporal optical and thermal satellite images. *Mapp. J.* 166, 1–9.

Kim, S. Y., Kwon, D. Y., Jang, A., Ju, Y. K., Lee, J. S., and Hong, S. (2023). A review of UAV integration in forensic civil engineering: From sensor technologies to geotechnical, structural and water infrastructure applications. *Measurement* 224, 113886. doi: 10.1016/j.measurement.2023.113886

Koch, T., Körner, M., and Fraundorfer, F. (2019). Automatic and semantically-aware 3D UAV flight planning for image-based 3D reconstruction. *Remote Sens.* 11, 1550. doi: 10.3390/rs11131550

Labuz, T. A. (2015). Environmental impacts—coastal erosion and coastline changes. *Second Assess. Climate Change Baltic Sea basin.* Editors: H. J. Bolle, M. Menenti and S. I. Rasool, 381–396. doi: 10.1007/978-3-319-16006-1_20

Lambert, S. E., and Parrish, C. E. (2023). Refraction correction for spectrally derived bathymetry using UAS imagery. *Remote Sens.* 15, 3635. doi: 10.3390/rs15143635

Lange, A. M., Fiedler, J. W., Merrifield, M. A., and Guza, R. T. (2023). UAV video-based estimates of nearshore bathymetry. *Coast. Eng.* 185, 104375. doi: 10.1016/j.coastaleng.2023.104375

Lee, C. H., Liu, L. W., Wang, Y. M., Leu, J. M., and Chen, C. L. (2022). Drone-based bathymetry modeling for mountainous shallow rivers in Taiwan using machine learning. *Remote Sens.* 14, 3343. doi: 10.3390/rs14143343

Lee, D. S., Storey, J. C., Choate, M. J., and Hayes, R. W. (2004). Four years of Landsat-7 on-orbit geometric calibration and performance. *IEEE Trans. Geosci. Remote Sens.* 42, 2786–2795. doi: 10.1109/TGRS.2004.836769

Legleiter, C. J., Roberts, D. A., and Lawrence, R. L. (2009). Spectrally based remote sensing of river bathymetry. *Earth Surface Processes Landforms* 34, 1039–1059. doi: 10.1002/esp.1787

Lin, Q., Vesecky, J. F., and Zebker, H. A. (1994). Comparison of elevation derived from Insar data with DEM over large relief terrain. *Int. J. Remote Sens.* 15, 1775–1790. doi: 10.1080/01431169408954208

Lingua, A. M., Maschio, P., Spadaro, A., Vezza, P., and Negro, G. (2023). Iterative refraction-correction method on mvs-sfm for shallow stream bathymetry. *Int. Arch. Photogrammetry Remote Sens. Spatial Inf. Sci.* 48, 249–255. doi: 10.5194/isprs-archives-XLVIII-1-W1-2023-249-2023

Lubczonek, J., Kazimierski, W., Zaniewicz, G., and Lacka, M. (2021). Methodology for combining data acquired by unmanned surface and aerial vehicles to create digital bathymetric models in shallow and ultra-shallow waters. *Remote Sens.* 14, 105. doi: 10.3390/rs14010105

Lyzenga, D. R. (1978). Passive remote sensing techniques for mapping water depth and bottom features. *Appl. optics* 17, 379–383. doi: 10.1364/AO.17.000379

Lyzenga, D. R. (1981). Remote sensing of bottom reflectance and water attenuation parameters in shallow water using aircraft and Landsat data. *Int. J. Remote Sens.* 2, 71–82. doi: 10.1080/01431168108948342

Lyzenga, D. R., Malinas, N. P., and Tanis, F. J. (2006). Multispectral bathymetry using a simple physically based algorithm. *IEEE Trans. Geosci. Remote Sens.* 44, 2251–2225. doi: 10.1109/TGRS.2006.872909

Mandlburger, G. (2019). Through-water dense image matching for shallow water bathymetry. *Photogrammetric Eng. Remote Sens.* 85, 445–455. doi: 10.14358/PERS.85.6.445

Mandlburger, G., Kölle, M., Nübel, H., and Sörgel, U. (2021). BathyNet: a deep neural network for water depth mapping from multispectral aerial images. *PFG-Journal Photogrammetry Remote Sens. Geoinformation Sci.* 89, 71–89. doi: 10.1007/s41064-021-00142-3

McFeeters, S. K. (1996). The use of the Normalized Difference Water Index (NDWI) in the delineation of open water features. *Int. J. Remote Sens.* 17, 1425–1432. doi: 10.1080/01431169608948714

Mulsow, C., Kenner, R., Bühler, Y., Stoffel, A., and Maas, H. G. (2018). Subaquatic digital elevation models from UAV-imagery. *Int. Arch. Photogrammetry Remote Sens. Spatial Inf. Sci.* 42, 739–744. doi: 10.5194/isprs-archives-XLII-2-739-2018

Muzirafuti, A., Barreca, G., Crupi, A., Faina, G., Paltrinieri, D., Lanza, S., et al. (2020). The contribution of multispectral satellite image to shallow water bathymetry mapping on the Coast of Misano Adriatico, Italy. *J. Mar. Sci. Eng.* 8, 126. doi: 10.3390/jmse8020126

Neeman, N., Servis, J. A., and Naro-Maciel, E. (2015). *Conservation issues: Oceanic ecosystems. Reference Module in Earth Systems and Environmental Sciences* (Amsterdam, The Netherlands: Elsevier). doi: 10.1016/B978-0-12-409548-9.09198-3

Nex, F., Armenakis, C., Cramer, M., Cucci, D. A., Gerke, M., Honkavaara, E., et al. (2022). UAV in the advent of the twenties: Where we stand and what is next. *ISPRS J. Photogrammetry Remote Sens.* 184, 215–242. doi: 10.1016/j.isprsjprs.2021.12.006

Niemeyer, J., and Sörgel, U. (2013). Opportunities of airborne laser bathymetry for the monitoring of the sea bed on the Baltic Sea coast. *Int. Arch. Photogrammetry Remote Sens. Spatial Inf. Sciences; XL-7/W2* 40, 179–184. doi: 10.5194/isprsarchives-XL-7-W2-179-2013

Niroumand-Jadidi, M., and Vitti, A. (2016). Optimal band ratio analysis of WorldView-3 imagery for bathymetry of shallow rivers (case study: Sarca River, Italy). *Int. Arch. Photogrammetry Remote Sens. Spatial Inf. Sci.* 41, 361–364. doi: 10.5194/isprs-archives-XLI-B8-361-2016

Ozdogan, N., Sefercik, U. G., Kilinc, Y., Caliskan, E., and Atalay, C. (2021). Determination of water quality by unmanned aerial vehicle data and analysis of physico-chemical parameters: case study aydınlar (Gülüç) stream. *Eur. J. Sci. Technol.* 23, 572–582. doi: 10.31590/ejosat.887105

Philpot, W. D. (1989). Bathymetric mapping with passive multispectral imagery. *Appl. Optics* 28, 1569–1578. doi: 10.1364/AO.28.001569

Pushparaj, J., and Hegde, A. V. (2017). Estimation of bathymetry along the coast of Mangaluru using Landsat-8 imagery. *Int. J. Ocean Climate Syst.* 8, 71–83. doi: 10.1177/1759313116679672

Randazzo, G., Barreca, G., Cascio, M., Crupi, A., Fontana, M., Gregorio, F., et al. (2020). Analysis of very high spatial resolution images for automatic shoreline extraction and satellite-derived bathymetry mapping. *Geosciences* 10, 172. doi: 10.3390/geosciences10050172

Rossi, L., Mammi, I., and Pelliccia, F. (2020). UAV-derived multispectral bathymetry. *Remote Sens.* 12, 3897. doi: 10.3390/rs12233897

Santos, D., Abreu, T., Silva, P. A., and Baptista, P. (2023). Georeferencing of UAV imagery for nearshore bathymetry retrieval. *Int. J. Appl. Earth Observation Geoinformation* 125, 103573. doi: 10.1016/j.jag.2023.103573

Sefercik, U. G., Alkan, M., Buyuksalih, G., and Jacobsen, K. (2013). Generation and validation of high-resolution DEMs from Worldview-2 stereo data. *Photogrammetric Rec.* 28, 362–374. doi: 10.1111/phor.12038

Sefercik, U. G., Kavzoglu, T., Cölkesen, I., Nazar, M., Oztürk, M. Y., Adali, S., et al. (2023a). 3D positioning accuracy and land cover classification performance of multispectral RTK UAVs. *Int. J. Eng. Geosci.* 8, 119–128. doi: 10.26833/ijeg.1074791

Sefercik, U. G., Kavzoglu, T., Nazar, M., Atalay, C., and Madak, M. (2022). Creation of a virtual tour.Exe utilizing very high-resolution RGB UAV data. *Int. J. Environ. Geoinformatics* 9, 151–160. doi: 10.30897/ijegeo.1102575

Sefercik, U. G., and Nazar, M. (2023b). Consistency analysis of RTK and Non-RTK UAV DSMs in vegetated areas. *IEEE J. Selected Topics Applied Earth Observations Remote Sens.* 16, 5759–5768. doi: 10.1109/JSTARS.2023.3288947

Slocum, R. K., Parrish, C. E., and Simpson, C. H. (2020). Combined geometric-radiometric and neural network approach to shallow bathymetric mapping with UAS imagery. *ISPRS J. Photogrammetry Remote Sens.* 169, 351–363. doi: 10.1016/j.isprsjprs.2020.09.002

Specht, M., Specht, C., Szafran, M., Makar, A., Dąbrowski, P., Lasota, H., et al. (2020). The use of USV to develop navigational and bathymetric charts of yacht ports on the example of National Sailing Centre in Gdańsk. *Remote Sens.* 12, 2585. doi: 10.3390/rs12162585

Specht, M., Szostak, B., Lewicka, O., Stateczny, A., and Specht, C. (2023). Method for determining of shallow water depths based on data recorded by UAV/USV vehicles and

processed using the SVR algorithm. *Measurement* 221, 113437. doi: 10.1016/j.measurement.2023.113437

Specht, M., Wiśniewska, M., Stateczny, A., Specht, C., Szostak, B., Lewicka, O., et al. (2022). Analysis of methods for determining shallow waterbody depths based on images taken by unmanned aerial vehicles. *Sensors* 22, 1844. doi: 10.3390/s22051844

Starek, M. J., and Giessel, J. (2017). "Fusion of uas-based structure-from-motion and optical inversion for seamless topo-bathymetric mapping," in *2017 IEEE international geoscience and remote sensing symposium (IGARSS)*. 2999–3002. doi: 10.1109/IGARSS.2017.8127629

Stumpf, R. P., Holderied, K., and Sinclair, M. (2003). Determination of water depth with high-resolution satellite imagery over variable bottom types. *Limnol. Oceanogr.* 48, 547–556. doi: 10.4319/lo.2003.48.1_part_2.0547

Teixeira, A. A., Mendes Júnior, C. W., Bredemeier, C., Negreiros, M., and Aquino, R. D. S. (2020). Evaluation of the radiometric accuracy of images obtained by a Sequoia multispectral camera. *Engenharia Agrícola* 40, 759–768. doi: 10.1590/1809-4430-eng.agric.v40n6p759-768/2020

Tewinkel, G. G. (1963). Water depths from aerial photographs. *Photogrammetric Eng.* 26, 1037–1042.

Tinkham, W. T., and Swayze, N. C. (2021). Influence of Agisoft Metashape parameters on UAS structure from motion individual tree detection from canopy height models. *Forests* 12, 250. doi: 10.3390/f12020250

Topaloglu, B. (2016). "Sponges of the Sea of Marmara with a New Record for Turkish Sponge Fauna," in *The Sea of Marmara Marine Biodiversity, Fisheries, Conservation and Governance*. Eds. E. Özsoy, M. N. Cagatay, N. Balkis, N. Balkis and B. Öztürk (Turkish Marine Research Foundation, Istanbul, Turkey), 418–427.

Toro, F. G., and Tsourdos, A. (2018). *UAV or Drones for Remote Sensing Applications* (Basel, Switzerland: MDPI-Multidisciplinary Digital Publishing Institute). doi: 10.3390/books978-3-03897-112-2

United Nations (2017). "Factsheet: people and oceans," in *Proceedings of the Ocean Conference*. 1–7. Available at: https://sustainabledevelopment.un.org/content/documents/Ocean_Factsheet_People.pdf.

Wang, C. K., and Philpot, W. D. (2007). Using airborne bathymetric lidar to detect bottom type variation in shallow waters. *Remote Sens. Environ.* 106, 123–135. doi: 10.1016/j.rse.2006.08.003

Westaway, R. M., Lane, S. N., and Hicks, D. M. (2000). The development of an automated correction procedure for digital photogrammetry for the study of wide, shallow, gravel-bed rivers. *Earth Surface Processes Landforms: J. Br. Geomorphological Res. Group* 25, 209–226. doi: 10.1002/(SICI)1096-9837(200002)25:2%3C209::AID-ESP84%3E3.0.CO;2-Z

Westaway, R. M., Lane, S. N., and Hicks, D. M. (2001). Remote sensing of clear-water, shallow, gravel-bed rivers using digital photogrammetry. *Photogrammetric Eng. Remote Sens.* 67, 1271–1282.

Westoby, M. J., Brasington, J., Glasser, N. F., Hambrey, M. J., and Reynolds, J. M. (2012). Structure-from-Motion'photogrammetry: A low-cost, effective tool for geoscience applications. *Geomorphology* 179, 300–314. doi: 10.1016/j.geomorph.2012.08.021

Wlodarczyk-Sielicka, M., and Stateczny, A. (2016). Comparison of selected reduction methods of bathymetric data obtained by multibeam echosounder. *Baltic Geodetic Congress (BGC Geomatics)* pp, 73–77. doi: 10.1109/BGC.Geomatics.2016.22

Woodget, A. S., Carbonneau, P. E., Visser, F., and Maddock, I. P. (2015). Quantifying submerged fluvial topography using hyperspatial resolution UAS imagery and structure from motion photogrammetry. *Earth surface processes landforms* 40, 47–64. doi: 10.1002/esp.3613

Xu, H. (2006). Modification of normalised difference water index (NDWI) to enhance open water features in remotely sensed imagery. *Int. J. Remote Sens.* 27, 3025–3033. doi: 10.1080/01431160600589179

Zhu, J., Hu, P., Zhao, L., Gao, L., Qi, J., Zhang, Y., et al. (2020). Determine the stumpf 2003 model parameters for multispectral remote sensing shallow water bathymetry. *J. Coast. Res.* 102, 54–62. doi: 10.2112/SI102-007.1

Zielinski, O. (2021). "The History and Future of the Secchi Disk," in *Angelo Secchi and Nineteenth Century Science: The Multidisciplinary Contributions of a Pioneer and Innovator*. Eds. I. Chinnici and G. Consolmagno (Springer, Cham, Switzerland), 215–224. doi: 10.1007/978-3-030-58384-2_13